Experimental Constraints on the Impact of Shear Strain Rate on Early Crystallization Dynamics and Residual Glass Composition: Implication for Magma Evolution in Natural Systems

Original:

Musu, A., Vetere, F., Griffiths, T., Petrelli, M., Corsaro, R.A., Pisello, A., et al. (2026). Experimental Constraints on the Impact of Shear Strain Rate on Early Crystallization Dynamics and Residual Glass Composition: Implication for Magma Evolution in Natural Systems. JOURNAL OF PETROLOGY [10.1093/petrology/egag015].

Published:

DOI: http://doi.org/10.1093/petrology/egag015

Experimental constraints on the impact of shear strain rate on early crystallization dynamics and residual glass composition: implication for magma evolution in natural systems

Alessandro Musu*[1,2]**,** *Francesco Vetere*[3], *Thomas Griffiths*[1], *Maurizio Petrelli*[4], *Rosa Anna Corsaro*[5], *Alessandro Pisello*[4], *Stefano Peres*[1], *Diego Perugini*[4], *Luca Caricchi*[2]

1) Department of Lithospheric Research, University of Vienna, UZA2, Josef-Holaubek-Platz 2, 1090 Vienna, Austria.

2) Department of Earth Sciences, University of Geneva, Rue des Maraîchers 13, CH-1205 Geneva, Switzerland.

3) Department of Physical Sciences, Earth and Environment (DSFTA), University of Siena, Via Laterina, 8, 53100 Siena, Italy.

4) Department of Physics and Geology, University of Perugia, Piazza dell'Università, 1, 06123 Perugia, Italy.

5) Istituto Nazionale di Geofisica e Vulcanologia, Osservatorio Etneo-Sezione di Catania, Catania, Italy.

* Corresponding author: Alessandro Musu, e-mail: musua93@univie.ac.at Tel.: + 39 380 437 2226

Key words: crystal zoning; crystallisation kinetics; eruptive dynamics; experimental petrology; shear strain rate.

ABSTRACT

Crystallisation processes in magmatic plumbing systems strongly influence magma rheology and eruptive styles. The presence of a deformation field in magma storage regions and transport systems can greatly affect crystal nucleation and growth. Here we present new experimental results on the effect of shear strain rates ($\dot{\Upsilon}$) on texture, crystal zoning patterns, mineral phase proportion (plagioclase, clinopyroxene, olivine, and oxides), and residual glass composition. The experiments, five in total, were carried out using natural trachybasalts under controlled temperature conditions at atmospheric pressure. The main experiment has been initially conducted at 1130 °C under a shear strain rate gradient ($1s^{-1}$ – $0s^{-1}$, from the rotating spindle to crucible walls) using a Concentric Cylinder Apparatus. Then, the deformation has been removed and minerals continued to evolve under temperature oscillations (1170 – 1130 °C). The main rationale behind our approach is to demonstrate the impact of deformation on early crystallization and the subsequent evolution of the system, even after deformation ceases to be effective. In natural settings, such conditions may arise during conduit dynamics, lava flow emplacement and during the development of a shallow magmatic system. Major element analyses and elemental maps were analysed using custom-built unsupervised and supervised machine learning algorithms (e.g., Hierarchical Clustering and Random Forest) to quantify how the area proportions of different chemical zoning patterns vary with inferred $\dot{\Upsilon}$. The effect of $\dot{\Upsilon}$ on nucleation, growth and mineral phase proportions was quantitatively investigated through shape and crystallographic preferred orientation analysis. The experimental results demonstrate how a small increase in $\dot{\Upsilon}$ can lead to a significant increase in nucleation rate and thus in crystal number density. While this general relationship has been observed in previous studies (Vona and Romano, 2013; Kolzenburg *et al.,* 2017; Vetere *et al.,* 2017, Mollo *et al.,* 2024), our results demonstrate how these changes directly influence growth competition among different mineral phases, leading to measurable variations in their growth rates, final mineral phase proportions, and residual melt composition. The application of our results to the February-April 2021 eruptive sequence of Mt. Etna reveals that the chemical variability observed in our experiments is in the same range as that observed at Mt. Etna during the studied eruptive sequence. This underlines how different $\dot{\Upsilon}$ (e.g., different magma ascent rates) can provide a major contribution to the chemical variability of the erupted products.

1 INTRODUCTION

Volcanic eruptions have the potential to cause damage to human life and activities (Kandlbauer *et al.*, 2013; Freire *et al.*, 2019; Malawani *et al.*, 2021; Mani *et al.*, 2021; Cassidy and Mani, 2022; Papale *et al.*, 2022). Basaltic volcanoes account for the majority of subaerial annual volcanic discharge (over 70%, Simkin *et al.*, 1994; Spina *et al.*, 2019) and can exhibit a wide range of eruptive activity, from less energetic effusive eruptions, through mildly explosive events (e.g., Strombolian activity and lava fountains), up to highly explosive Plinian episodes (Sable et al., 2006; Simakin and Bindeman, 2008; Freda et al., 2011; Abbott et al., 2021; Bamber et al., 2022). Reconstructing pre- and syn-eruptive dynamics responsible for shifts in eruptive style is of primary importance for hazard assessment at basaltic volcanoes. A key factor modulating eruptive style variability is magma rheology (Cassidy *et al.*, 2018; La Spina *et al.*, 2021), which can be strongly influenced by crystallization processes (Lejeune and Richet, 1995; Cashman and Blundy, 2000; Caricchi *et al.*, 2007; Giordano *et al.*, 2008; Arzilli *et al.*, 2019; Bamber *et al.*, 2022; Vetere *et al.*, 2022). Crystal nucleation and growth can occur on very short timescales, down to minute, during ascent (Cashman and Blundy, 2000; La Spina *et al.*, 2015; Arzilli *et al.*, 2019; Mollo *et al.*, 2022), strongly affecting viscosity and explosivity (Vona *et al.*, 2011; Baker *et al.*, 2012; Szramek, 2016; Moitra *et al.*, 2018; Bamber *et al.*, 2020).

Among the processes that promote crystallization, in addition to cooling and degassing (Brandeis and Jaupart, 1986; Blundy and Cashman, 2001; Shea and Hammer, 2013; Mollo and

Hammer, 2017), deformation during magma transport can also play a significant role. Experimental studies demonstrate that shear strain rate ($\dot{\Upsilon}$) can directly influence crystal nucleation and growth, thereby affecting magma texture and rheology (Kouchi *et al.*, 1986; Ishibashi and Sato, 2007; Vona *et al.*, 2011; Vona and Romano, 2013; Kolzenburg *et al.*, 2018a; Di Fiore *et al.*, 2022, 2024; Vetere *et al.*, 2024). In magmatic systems, $\dot{\Upsilon}$ can range from about 7x10 s^{-1} to 10^{-9} s^{-1} and deformation is ubiquitous during magma emplacement, storage, and transfer (Nicolas and Ildefonse, 1996; Papale, 1999; Piombo and Dragoni, 2009; Cashman *et al.*, 2013; Kolzenburg *et al.*, 2018a, 2018b). Understanding and quantifying the role of deformation in the chemical and textural evolution of magmas is therefore crucial for reconstructing pre- and syn-eruptive dynamics. This also allows discrimination between features linked to deformation-driven crystallization and those related to other petrologic processes. While several studies have investigated the role of deformation on magma crystallization and rheology (Kouchi *et al.*, 1986; Vona *et al.*, 2011; Vona and Romano, 2013; Vetere *et al.*, 2019; Di Fiore *et al.*, 2022; Frontoni *et al.*, 2022; Kolzenburg *et al.*, 2022), knowledge of the impact of the initial effects of deformation on the subsequent textural and chemical evolution of magmas (e.g., crystal zoning, phase proportions, and residual melt composition) is still lacking.

Here we present an experimental study that investigates the impact of $\dot{\Upsilon}$ on crystal zoning patterns, mineral phase proportions, and residual melt compositions through high-temperature crystallization experiments on trachybasaltic melts from Mt. Etna (Italy). Mt. Etna is among the most active mafic volcanoes in the world (Branca *et al.*, 2004; Cappello *et al.*, 2013). The volcano shows a wide range of eruptive styles, and since the late 20th century has shown a marked increase in explosivity (Behncke and Neri, 2003; Branca and Del Carlo, 2005; Cappello *et al.*, 2013). These characteristics make the products erupted from Mt. Etna perfect candidates for investigating crystallisation processes, their effect on rheology and eruptive style, providing a framework to compare experimental and natural samples.

Five specifically designed crystallization experiments have been conducted under static and dynamic conditions, applying a deformation field in the sample using a concentric cylinder apparatus. This setup allowed different melt regions to experience distinct strain rates within the same experimental run, while additional static runs served as controls to separate deformation effects from purely thermal ones. Crystallographic Preferred Orientation (CPO, Appendix 1) and Shape preferred Orientation (SPO, Appendix 1) was used as a proxy for relative $\dot{\Upsilon}$ variation within dynamic experiments. Finally, we place the experimental results in the context of natural products from the February-April 2021 eruptive sequence of Mt. Etna, with the aim of constraining the possible role of ascent dynamics in residual melt evolution.

2 MATERIALS AND METHODS

2.1 Experimental Strategy

Five crystallization experiments were conducted at the Department of Physics and Geology, University of Perugia, including two main runs under both dynamic and static conditions. Specifically, three dynamic experiments (Md, Sd2, and Sd3) were performed under constant applied deformation, while two static experiments (Ms and Ss1) were conducted without deformation. In the main experimental runs (Md and Ms), temperature oscillations were imposed.

The Md run was performed under constant deformation conditions using a Concentric Cylinder Apparatus (Dingwell and Virgo, 1987, 1988; De Campos *et al.*, 2011) until a peak in viscosity was achieved. The Concentric Cylinder Apparatus, described in detail below, allows a Taylor-Couette flow to be established within the sample, with the $\dot{\Upsilon}$ decreasing from the spindle to the walls of the crucible (Taylor, 1923). This set-up provides us with a sample that experienced identical thermal fluctuations (ΔT = 40°C) throughout, but at different $\dot{\Upsilon}$. The Ms experiment mimics Md, in static conditions. A temperature fluctuation of 40°C was chosen to represent a broad thermal range below the liquidus temperature of clinopyroxene and plagioclase, as calculated with MELTS (~1195°C for both phases; Gualda et al., 2012). This ensured sufficiently distinct thermal conditions to allow for potential differences in crystal chemistry as derived, for example, during convection or from repeated injections of new magmas in a shallow reservoir. Additionally, temperature cycling can promote crystal growth, facilitating the formation of crystals large enough for compositional analysis (Mills et al., 2011; Mills and Glazner, 2013; Vetere et al., 2024). Further details on the experimental apparatus, sample preparation, Taylor-Couette flow, and analytical methods are available in Appendix 1.

The three additional snapshot experiments (Ss1, Sd2, and Sd3) were performed to investigate the early stages of crystallisation and to assess the effects of temperature oscillations on the resulting textures. Each snapshot experiment replicated the main experimental setup, with the final products quenched at different stages of the run. Further information on both the main and snapshot experiments is provided in Section 2.3, "Experimental setup". The adopted strategy was chosen to investigate the role of deformation in early crystallization processes and subsequent textural and chemical evolution of magmas. In natural settings, the investigated conditions may arise during the development of a shallow magmatic system, establishment of conduit flow, or associated with lava emplacement. For example, early crystallization may occur during ascent and melt migration, where portions of an emplaced magma batch at shallow levels reach high crystallinity, effectively inhibiting further deformation, while thermal oscillations continue due to the repeated injection of fresh magma into the system or general convective movements.

2.2 Starting Material

We used trachybasaltic scoriae from the 2002-03 eruption of Mt. Etna as a starting material. The scoriae were collected from scoria cones on the South flank of the South-East crater (SEC). The products emitted from the southern eruptive fissure during the 2002-03 flank eruption are among the most primitive erupted in recent history (Andronico *et al.*, 2005). This allows us to perform crystallisation experiments with the closest possible composition to the source magma that fuels recent volcanic activity at Mt. Etna.

The natural trachybasaltic scoriae present a mineral assemblage of plagioclase (Pl), clinopyroxene (Cpx), olivine (Ol) and oxides (Ox) phenocrysts with a microlitic groundmass mainly composed of Pl and Cpx, with minor Ol and Ox (Fig. S1). The original bulk rock composition of the starting material is reported in Andronico et al. (2005, Type 2 magma composition erupted by the S fissure during the 2002 Mt. Etna eruption). A homogeneous starting glass was produced from natural scoriae following the procedure described in Appendix 1. The chemical composition of the starting glass is reported in Table 1.

2.3 Experimental setup

About 125 grams of homogeneous glass was placed in a large $Pt_{80}Rh_{20}$ cylindrical crucible (height: 7 cm; inner diameter: 3.7 cm; wall thickness: 0.1 cm) and remelted at 1400°C in a Gero HTRV 70-250/18 High-temperature furnace, at the oxygen fugacity (fO_2) of air. An Al_2O_3 rod, covered with a $Pt_{80}Rh_{20}$-head cylindrical spindle (diameter: 1.2 cm), attached to an Anton Paar RheolabQC rheometer, was placed at the centre of the crucible, and immersed in the melt to a depth of 3.5 cm (Fig. 1a). In all the five experiments, the spindle was inserted into the melt. However, in the static runs it remained stationary, while in the dynamic ones it was rotated at a constant speed (Fig. 1b). This setup was used to isolate the effect of deformation on crystallization processes. Inserting the spindle in the static experiments also enabled us to look for potential heterogeneous nucleation at the melt–spindle interface.

In the Md experiment, the spindle was set to rotate at constant speed (Ω_1 = 4.24 min^{-1} or 0.45 rad/s), applying to the sample a constant shear strain rate ($\dot{\Upsilon}$) of 1 s^{-1} at the spindle-melt boundary, which is the same order of magnitude as those expected in volcanic conduits (10^{-1}–10^{1} s^{-1}; Papale, 1999; Kolzenburg et al., 2018a), lava flows (2.5–0.001 s^{-1}; Cashman et al., 2013; Kolzenburg et al., 2018a), or during magma migration from deep to shallow reservoirs (up to 1s^{-1}, Rubin, 1995; Petrelli et al., 2018; Albert et al., 2020). However, this value is not representative of the much higher shear strain rates expected during highly explosive eruptions (e.g., up to 70 s^{-1} during Plinian events, Papale, 1999; Kolzenburg et al., 2018a), nor of the much lower strain rates potentially occurring in high-viscosity magma storage regions, which may reach values as low as 10^{-9} s^{-1} (Nicolas and Ildefonse, 1996; Kolzenburg et al., 2018a).

The Md experiment began by re-melting the starting material at 1400°C for about 30 minutes, after which the spindle was placed into the melt. After an additional 15 minutes at 1400°C, rotation was started ($\dot{\Upsilon}$ = 1s^{-1}). The set-up remained at the temperature of 1400°C with the spindle rotating for a further 15 minutes after which the temperature was lowered to the first dwell temperature of 1170°C at the maximum achievable cooling rate of our experimental setup, ~12-13°C/min. After one hour at 1170°C (dwell-T_1), the temperature was decreased to 1130°C (dwell-T_2) with cooling rate of 1°C/min and held constant for 1 h. At the end of this step the spindle was stopped due to the high viscosity reached within the sample (over 10^5 Pas). Then the temperature was cycled 10 times between the two dwell temperatures (with a dwell-ΔT = 40°C). Each cycle consisted of: (i) lowering the temperature to dwell-T_2 (1130°C) with a cooling rate of 1°/min, (ii) 1h at dwell-T_2, (iii) raising the temperature back to dwell-T_1 with a heating rate of 1°C/min, (iv) 1h at dwell-T_1. At the end of the 10 cycles, the sample was left 48h at the average temperature of 1150°C (dwell-T_3), with the aim of forming final crystal rims in equilibrium with the melt (Fig. 1c). The estimated uncertainty in T estimates within the crucible is of about ± 3° C (Appendix 1). At the end of the experiments, the crucible was quenched in air, reaching the estimated glass transition temperature (~681 °C) in about 8 min. The spindle was left inserted into the sample for all experiments.

The Ms experiment followed an identical temperature-time path, but the spindle remained stationary after insertion.

The three additional snapshot experiments were performed by replicating the original dynamic and static experiments, with the final products quenched at earlier stages of the experimental run. Specifically: (i) in Ss1 we replicated Ms, quenching the system after the first step at 1130 °C, prior to the onset of temperature oscillations (Fig. 1d); (ii) in Sd2, we repeated Ss1, but under dynamic conditions (Fig. 1e); and (iii) in Sd3, we duplicated Sd2, but we quenched the system earlier, immediately after the 1170 °C step (Fig. 1f).

2.4 Taylor-Couette flow

In the concentric cylinder geometry used in the described experiment, with the outer cylinder (crucible) fixed (angular velocity, $\Omega_2 = 0$ rad/s) and the inner cylinder (spindle) rotating at constant angular velocity ($\Omega_1 = 0.45$ rad/s, Fig. 1b), a Taylor-Couette flow is established in the high-temperature melt that fills the gap between the two cylinders (Taylor, 1923; Donnelly, 1991; Perugini *et al.*, 2008; Morgavi *et al.*, 2015; Cagney and Balabani, 2019). In our specific configuration we have the establishment of an inhomogeneous flow within the crucible, with flow velocity (u) and $\dot{\Upsilon}$ decreasing from the rotating spindle towards the crucible walls (Fig. 1b; Mondy *et al.*, 1994; Toorman, 1994; Cheng *et al.*, 2014; Sarabian *et al.*, 2019). Further details on the melt flow within the experiment and on the calculation of flow velocity and initial $\dot{\Upsilon}$ distribution within the sample are provided in Appendix 1.

Here, we assume that the estimated $\dot{\gamma}$ distribution (Fig. 1b; Appendix 1) is only present in the sample until crystallisation begins. As the sample begins to crystallise, the presence of zones with variable number of particles, different viscosities, and different crystal number densities, leads to the development of inhomogeneities within the sample (Appendix 1; Shinbrot *et al.*, 1999; Morgavi *et al.*, 2013, 2015; Perugini, 2021; Feldmann *et al.*, 2023), complicating the modelling of $\dot{\gamma}$. For this reason, to correlate zoning-patterns with the relative $\dot{\gamma}$ degree, we quantify the SPO and CPO strength in different zones of the experimental sample.

2.5 Sample preparation for textural and chemical analysis

The post-run products were drilled, and a cylindrical core (30 mm diameter × 60 mm length) was extracted. All the cylindrical cores were sectioned perpendicular to the rotation axis at a depth of approximately 20 mm from the sample surface. For the Md experiment two sections were extracted at depths of 20 mm (Md-s28107) and 10 mm (Md-s28106) to investigate potential chemical variations in the third dimension (Fig. S2). As shown later, the Ms run product (Ms-s12101) exhibits a homogeneous crystal distribution throughout the sample. Therefore, a detailed study of the textural and chemical variations of the mineral population was conducted only on Md, where significant textural variations were observed as a function of the inferred $\dot{\gamma}$.

2.6 Microstructural Analysis

The final products of Ms and snapshot experiments were analysed qualitatively by SEM Backscattered Electron (BSE) imaging to determine which phases crystallised in each step.

Electron Backscatter Diffraction (EBSD) scans were collected to segment the different mineral phases contained in the Md experiment (sample Md-s28107), and to quantify the crystal SPO and CPO strength. EBSD scans deliver accurate mineral phase segmentation, as the technique is able to automatically separate individual crystals based on both crystal structure and orientation (Berger *et al.*, 2011). In addition, determining CPO and SPO (Demurtas *et al.*, 2019) enables us to qualitatively infer the relative $\dot{\Upsilon}$ in different regions of the sample.

We acquired large EBSD maps (area, A > 1.8 mm^2) on sample Md-s28107 (20 mm sectioning depth) from three different areas:

- scan-01: (1.82 mm^2, 0.85 µm step size) was acquired close to the spindle (extending from ~ 0.3 to ~ 1.3 mm away from the spindle)

- scan-02 and -03: (1.9 mm^2 and 3.92 mm^2, both 2.3 µm step size) were acquired far from the spindle at similar radial distances (both extending from ~ 6 to ~ 7.3 mm away from the spindle), but in areas presenting different microstructures.

2.6.1 EBSD analysis

EBSD analysis was carried out at the laboratory for field-emission scanning electron microscopy and focused ion beam applications at the Faculty of Geosciences, Geography and Astronomy, University of Vienna, using a FEI Quanta 3D field emission Scanning Electron Microscope (SEM) equipped with an EDAX Digiview V EBSD camera. The OIM DC v7.3.1 analysis software was used for data acquisition. The beam conditions used for the acquisition of all the EBSD scans were a 15 kV accelerating voltage and a spot size of 1.0 with a 1 mm aperture, corresponding to ~ 4 nA probe current. Additional details on EBSD analytical conditions and data processing are available in Appendix 1. All data processing was carried out using the MATLAB toolbox MTEX (Bachmann et al. 2010) version 5.11.2. Grains were reconstructed using a 15° misorientation angle threshold and minimum grain size of 4 (scan-01) or 2 (scans -02 and -03) pixels. CPO information was obtained for all scans by calculating orientation distribution functions (ODFs) for each mineral phase, using as input the grain mean orientations to prevent area weighting of the ODF, which might otherwise lead to 2D sectioning effects on the CPO data resulting from the SPO of anisotropically shaped grains. Note that for

CPO analysis, plagioclase twins are counted as separate grains. Texture strength was calculated using the texture index (also known as the J-index) of the whole ODF (Mainprice *et al.*, 2015), which ranges from 1 for a uniform orientation distribution to infinity for a single crystal.

2.6.2 Crystal size and SPO analysis

We estimated the crystal area fraction ($\varphi_{\mathrm{crystal}}$) and the crystal number density (N_A^{crystal}) for each mineral phase in each scan area directly from the EBSD data, using the fraction of the total number of EBSD pixels indexed as a given phase ($\varphi_{\mathrm{crystal}}$) and the number of reconstructed grains divided by the scan area (N_A^{crystal}). From these parameters we then estimated the characteristic crystal size (S_N^{crystal}) as:

$$S_N^{crystal} = \left(\frac{\varphi_{crystal}}{N_A^{crystal}}\right)^{0.5} \qquad (1)$$

And the volumetric number density (N_V^{crystal}) as:

$$N_V^{crystal} = \frac{N_A^{crystal}}{S_N^{crystal}} \qquad (2)$$

The strength of 2D Pl SPO (S_{spo}) was obtained from the orientation tensor derived from the best-fit ellipsoid long axis orientations of the segmented crystals and expressed as the normalized ratio between the two eigenvalues.

All size, number density, and shape-based analysis of plagioclase used grains merged along twin boundaries, to prevent twinning from affecting results (see Appendix 1).

2.6.3 Crystal size distribution

We investigate, for each scan, the crystal size distribution (CSD; Cashman and Marsh, 1988; Higgins, 2000; Armienti, 2008) of all three mineral phases contained in our experimental sample: plagioclase (Pl), clinopyroxene (Cpx) and Fe-spinel (Fe-Spl). The CSD was calculated using the software CSDCorrections (Higgins, 2000), this procedure calculates the true 3D-CSD, using correction for both the cut-section effect and the intersection probability (Higgins, 2000;

Mock and Jerram, 2005; Brugger and Hammer, 2010; Cashman, 2020; Okumura *et al.*, 2022). All the input parameters used for the CSD calculation are available in supplementary table ST1. The 3D crystal aspect ratio (or habit, expressed here as Short:Intermediate:Long axis of the crystal – S:I:L) used for CSD were estimated through ShapeCalc (Mangler *et al.*, 2022). In doing so, we assumed that all analysed crystals belonging to the same mineralogical phase have a similar 3D shape. More details on aspect ratio calculation and CSD are available in Appendix 2 and 1. To minimise the impact that areas containing crystals with a strong preferential orientation might have on the determination of the representative 3D aspect ratio (Okumura *et al.*, 2022), we calculated the 3D aspect ratio for each mineral phase in two different ways: (i) using the largest 1/3 of crystals from all three scans combined and (ii) using all crystals from scan-02 (which is the scan showing the least crystal preferential orientation). This procedure yielded two 3D aspect ratio estimates per mineral phase, resulting in two CSD curves for each phase. The difference between the two CSDs was minimal for all mineral phases, and we used an average between the two as the best fit CSD (Fig. S3). Further information on this procedure is also available in Appendix 2.

2.6.4 Calculating nucleation and growth rates

We estimate the maximum growth rate (G_{MAX}) and the average nucleation rate (J_M), for each mineral phase in relation to the main experiment duration (starting from the first step at 1170°C) using the approach of Hammer and Rutherford (Hammer and Rutherford, 2002; Couch *et al.*, 2003; Vona and Romano, 2013). G_{MAX} and J_M have then been calculated as:

$$G_{MAX} = \frac{(l \times w)^{0.5}}{2 \times \Delta t} \qquad (3)$$

and,

$$J_M = N_V / \Delta t \qquad (4)$$

Where Δt is the duration time of the experiment and the factor ½ used in the G_{MAX} formula accounts for the growth of the crystal in two opposite directions from its centre (Hammer and Rutherford, 2002; Vona and Romano, 2013).

The use of Eqs. 3 and 4, is optimal to calculate apparent J_M and G_{MAX} in our experimental conditions, where a linear log distribution of crystal sizes is not observed. This is because the growth rate (G) under our experimental conditions may not be constant with respect to time and size, making the use of CSD trends unreliable for determining accurate kinetic parameters (Mills and Glazner, 2013; Vona and Romano, 2013).

2.7 Chemical Analysis

Two samples from the Md experiment (Md-s28107 and Md-s28106, Appendix 1) were analysed by Electron Probe Micro Analyser (EPMA). Major element chemical analysis of all mineral phases (Pl, Cpx and Fe-Spl) and glass were acquired at different distances from the spindle using a JEOL 8200 Superprobe at the University of Geneva. For sample Md-s28107 (for which three large EBSD scans are available) we also acquired three EPMA-WDS chemical maps (> 500 x 500 µm), within each of the EBSD areas. The Pl analyses were conducted with a probe beam diameter (spot size) of 5 µm, an acceleration voltage of 15 kV and a probe current of 15 nA. Cpx and Fe-Spl analyses were conducted with a focused beam, a voltage of 15 kV and a beam current of 20 nA. The setup for glass analysis was a 10 µm spot size, a 15 kV voltage and a beam current of 6 nA. WDS maps (> 0.25 mm^2) were collected using a 1 µm pixel size (> 256000 pixels per map). For each map we measured 5 elements (Al_2O_3, CaO, FeO, MgO and TiO_2) with an analysis time of about 13 hours per map. The analytical conditions used for the chemical map were 15 kV, 50 nA and a dwell time of 150 ms.

Analyses of Pl and Cpx were filtered by removing all data with a total oxide content below 98% and above 102% and keeping only analyses delivering a cation per formula unit between 5.04 and 4.98 or between 4.04 and 3.98 for Pl and Cpx, respectively. For Fe-Spl, Fe^{3+}/Fe^{2+} have been estimated through stoichiometric calculation using OxyEMG (Ferracuti *et al.*, 2024), and all analyses fall within a valid compositional range.

All the EPMA point analyses are available in supplementary Table ST2. All the detailed analytical conditions and uncertainties are available in the EarthChem repository (https://doi.org/10.60520/IEDA/113368). Data filtering, transformation and normalization, coupled with robust cluster validation methods and outlier detection minimized the effect of analytical uncertainty on cluster identification (see section 2.8 "Hierarchical Clustering" and Appendix 3 for details).

2.8 Hierarchical Clustering

All the geochemical data collected for each mineral phase were analysed using a Hierarchical Clustering (HC) algorithm. Clustering methods are unsupervised machine learning techniques able to robustly group multivariate observations into meaningful and homogeneous clusters (Templ *et al.*, 2008; Rousseeuw and Hubert, 2011; Caricchi *et al.*, 2020; Musu *et al.*, 2023, 2025; Petrelli, 2023, 2024). This methodology helps us to identify groups of similar composition within and between crystals and it has the capability to track the variation in proportions of chemical clusters in the experimental products following the procedure described in Musu et al. (2023). The detailed procedure for the transformation and normalisation of the data, the application of the HC, the detection of outliers and the validation of the number of clusters are reported in Appendix 3. To summarise, the filtered geochemical data collected with EPMA were first transformed using the isometric log-ratio (ilr) transformation (Egozcue *et al.*, 2003; Boschetty *et al.*, 2022; Musu *et al.*, 2023; Petrelli, 2023), then normalised following the Media-MAD method (Templ *et al.*, 2008; Rousseeuw and Hubert, 2011; Eesa and Arabo, 2017; Musu *et al.*, 2023) and finally analysed using HC algorithms. HC was applied using the 'clusters' library in the open-source software R (R Core Team, 2021), using the Ward minimum variance linkage criteria (Ward Jr, 1963; Caricchi *et al.*, 2020; Musu *et al.*, 2023). Clustered data are available in supplementary table ST3.

2.8.1 Outlier detection

Once the clusters were uniquely identified we removed possible outliers from each cluster. In our specific case outliers are mainly related to observations acquired between two chemical zones or between two distinct phases.

To remove outliers, we calculated the Mahalanobis distance and marked as outliers the observations lying outside the 97.5 percentile range of the distribution (Musu *et al.*, 2023). The Mahalanobis distance was calculated as (Mahalanobis, 1936; Boschetty *et al.*, 2022; Musu *et al.*, 2023):

$$D_M(\vec{x}) = \sqrt{(\vec{x} - \vec{\mu})^T \; C^{-1} \; (\vec{x} - \vec{\mu})} \quad (5)$$

Where $\vec{x}$ is the matrix of all the observations within a single cluster, C is the estimator of the distribution centre location, and $\vec{\mu}$ is the covariance estimator. For the C and $\vec{\mu}$ estimators we replace the classic estimators (mean and covariance) with more robust estimates of location and dispersion such as median and co-median (Di Palma and Gallo, 2016) using the package “robustbase” in R (R Core Team, 2021).

We finally determine and validate the number of clusters for each phase following the approach proposed by Musu et al., 2023 and reported in appendix 3.

2.9 Elemental map segmentation

We visualised the distribution of clusters in two dimensions starting from the 2D EPMA chemical maps. We first quantified the raw chemical maps by calibrating them with quantitative points acquired within the maps using the open-source software XMapTools (Lanari *et al.*, 2014). To cluster the calibrated maps, we followed two different approaches: (i) re-performing HC analysis, for each mineral phase, on a new dataset consisting of all the map-pixel-compositions combined with the point analysis dataset (in this case we could only use the 5 oxides analysed in the maps to define the clusters); and (ii) by using the clustering data already obtained from the point analyses alone (but based on a larger number of chemical components) to train a map classifier using the Random Forest (RF) algorithm (Breiman, 2002; Petrelli *et al.*, 2020; Higgins *et al.*, 2022; Jorgenson *et al.*, 2022; Musu *et al.*, 2023; Petrelli, 2023, 2024), capable of quickly classifying each chemical map. A detailed comparison between the two techniques is available in Appendix 4. The two approaches produce comparable results; however, the maps obtained through the RF classifier result in less noisy cluster maps and in a clearer and more homogeneous characterization of areas with similar chemical composition. After extensive comparison and evaluation, we adopted the second approach, training the RF classifier on the HC results from point analyses. The model was then validated on a separate test dataset and subsequently applied to the chemical maps, assigning each pixel to its corresponding cluster. This procedure enabled the generation of 2D maps that illustrate the spatial distribution of the clusters across different areas of the experimental sample. A detailed description of the RF classifier, including its functioning and training, is provided in Appendix 4.

3 RESULTS

Most quantitative investigations (i.e., EBSD, CSD, and EPMA chemical maps) were performed on the Md experiment, which exhibits significant textural variations across areas subjected to different $\dot{\gamma}$ (Fig. 2a). Experiments Ms, Ss1, Sd2, and Sd3 were used for hypothesis testing and validation of the results. Unless explicitly stated otherwise, the results presented below refer to experiment Md and are presented hereafter following the same structure as in the Methods section.

Within sample Md-s28107 (Fig. S4), we distinguished three areas based on the crystal SPO and CPO strengths (S_{spo} and J_{ODF}; section 3.2). The area closest to the spindle displays a stronger SPO and CPO (particularly of Pl: Pl-$S_{spo} = 0.096$ and Pl-$J_{ODF} = 1.44$) and is interpreted as a high-$\dot{\Upsilon}$ domain. A second area, located further from the spindle, shows a weaker SPO and CPO (Pl-$S_{spo} = 0.077$ and Pl-$J_{ODF} = 1.25$) resulting in a lower inferred $\dot{\Upsilon}$. A third area, located at a similar radial distance from the spindle as the second area, exhibits no visible SPO and the weakest CPO (Pl-$S_{spo} = 0.074$ and Pl-$J_{ODF} = 1.17$), and is thus interpreted to represent the lowest $\dot{\Upsilon}$ domain. Detailed correlations between crystal shape and orientation are presented in Appendix 5.

We acquired an EBSD scan and an EPMA chemical map in each of these areas (scans 01-03 and maps 01-03; see sections 2.6 and 2.7). The three areas are presented in decreasing order of inferred $\dot{\Upsilon}$ (i.e., scan-01, scan-03, then scan-02) and are referred to as high-, low-, and lowest-$\dot{\Upsilon}$ domains (H$\dot{\Upsilon}$, L$\dot{\Upsilon}$, 0$\dot{\Upsilon}$). The lowest-$\dot{\Upsilon}$ domain (where the minimum CPO and SPO are recorded) have been normalised to 0 and represented as 0$\dot{\Upsilon}$.

3.1 Petrography

BSE imaging across all the experimental products enabled the identification of the principal petrological features. The Md experiment exhibits a mineral assemblage of Pl, Cpx and Fe-Spl, with marked variations in crystal size and orientation (Fig. 2a) moving away from the spindle. The Ms run displays the same mineral assemblage as Md but it features a homogeneous crystal distribution (Fig. 2b).

Among the snapshot experiments, Ss1 is almost entirely glassy, with a few Fe-spinel crystals dispersed throughout the sample (Fig. 2c). In contrast, Sd2 exhibits significantly stronger crystallization, with a mineral assemblage of Pl, Cpx and Fe-Spl (Fig. 2d). Sd2 also displays qualitatively the same variation in crystal sizes and orientation as experiment Md. Finally, Sd3 resulted in a homogeneous, crystal-free glass (Fig. S5).

The qualitative textural features of all the mineralogical phases in the Md run, are reported in Fig. 3, while BSE panoramas at fixed magnification for the three ϓ̇ domains are available in Fig. S6.

All over the sample, Pl crystals are elongated with a hopper to skeletal shape and exhibit two distinct zones. These zones consist of (i) a bright skeletal core with hollow section, partially or entirely filled by plagioclase with slightly lower BSE intensity (Fig. 3a) and (ii) a very dark overgrowth rim (Fig. 3a). The filled zones in the skeletal bright cores are sometimes homogenous and sometimes characterised by oscillatory zoning (Fig. 3a). Some plagioclase skeletal cores also present a sector-zoning-texture, with a slightly darker {001} sector. These darker sectors may be incompletely developed, showing voids or shallow surface indentations and they may be either homogenous or characterized by alternating light and dark layers (Fig. S7). As shown in Fig. 3a, sometimes the bright skeletal zones show evidence of resorption at the contact with the overgrowth rims. The Cpx phase presents a tabular to sub-equant shape and shows three texturally distinct zones, a euhedral dark core, an irregular bright mantle, and a final rim with intermediate BSE intensity (Fig. 3b). In few smaller Cpx a sector-zoning texture is also observed (Fig. S8). The final rim looks internally homogeneous all over the samples. Very minor, small, dark cpx fragments are also found incorporated within the overgrowth rims of the largest Cpx, mainly in scan-0ϓ̇. Only in Cpx that grew in the 0ϓ̇ area we observe complex and thin (< 1 µm) oscillatory zonation (Fig. 3b) between the resorbed bright mantle and the final rim. The maximum number of clearly distinguishable oscillatory zones is 8 (Fig. 3c). Fe-Spl are equant in shape and look homogeneous within the samples, with an idiomorphic to slightly rounded habit (Fig. 3d).

3.2 Mineral proportions, Shape and Crystallographic preferred orientations

3.2.1 Mineral phase distribution within the samples

Results for the mineral phase proportion within the three $\dot{\Upsilon}$ domains are displayed in the pie charts in Fig. 4b. The glass area increases with decreasing Pl CPO strength and inferred $\dot{\Upsilon}$, while Pl area shows the opposite trend. Fe-Spl and Cpx area percentage is almost constant across the three scans, although Cpx fraction shows a slight decrease in scan-L$\dot{\Upsilon}$ (Fig. 4).

3.2.2 Mineral SPOs

The SPOs of each mineral phase for each scan are shown as rose diagrams in Figure 5b, e and h, accompanied by quantitative Pl SPO strength (Pl-S_{spo}) values for each diagram. In general, the degree of orientation is stronger at higher inferred $\dot{\Upsilon}$ and weaker at lower inferred $\dot{\Upsilon}$. Among the mineral phases Pl generally shows a stronger degree of orientation, followed by Cpx and Spl.

3.2.3 Plagioclase CPO

In scan-H$\dot{\Upsilon}$, plagioclase shows a weak (texture index, J_{ODF} = 1.44) CPO which nonetheless clearly reflects the geometry of the applied experimental deformation (Fig. 5a, b and c). Plagioclase (100) poles are somewhat concentrated in a girdle aligned subparallel to the spindle surface, with a weak maximum subparallel to the shear direction. $(010)_{Pl}$ poles show a concentration normal to the spindle surface (radial to the spindle), while $(001)_{Pl}$ poles show a diffuse girdle with no clear maxima, again subparallel to the spindle surface (Fig. 5c). In scan-L$\dot{\Upsilon}$, the plagioclase CPO is even weaker (J_{ODF} = 1.25), and the CPO is much less clearly oriented with respect to experimental deformation (Fig. 5e, d and f). Nonetheless, diffuse $(100)_{Pl}$ and $(010)_{Pl}$ maxima are present within tens of degrees of their positions in scan-H$\dot{\Upsilon}$. The $(001)_{Pl}$ girdle of scan-H$\dot{\Upsilon}$ is replaced by a single weak $(001)_{Pl}$ maximum in scan-L$\dot{\Upsilon}$ (Fig. 5f). Scan-0$\dot{\Upsilon}$, with the weakest Pl texture index of 1.17, still shows a $(100)_{Pl}$ maximum approximately in the plane of the spindle surface but rotated from its positions in scan-Hϒ̇ and -Lϒ̇ (Fig. 5i). A subvertical $(010)_{Pl}$ maximum is also present, but $(010)_{Pl}$ poles are also found more frequently in other orientations compared to the previous scans. Finally, $(001)_{Pl}$ poles in scan-0ϒ̇ show almost no preferred orientation (Fig. 5i).

3.2.4 Clinopyroxene CPO

The clinopyroxene CPO (J_{ODF} = 1.09) in scan-Hϒ̇ is considerably weaker than that of plagioclase (Fig. 5). Nonetheless, slight concentrations of poles at positions related to experimental deformation are visible for scan-Hϒ̇, with subvertical diffuse $(100)_{Cpx}$ and $(010)_{Cpx}$ maxima, and a weak girdle of $(001)_{Cpx}$ poles subparallel to the spindle surface, with a maximum subparallel to the spindle rotation axis (Fig. 5c). In scan-Lϒ̇, the clinopyroxene CPO is only slightly weaker (J_{ODF} = 1.07), but, as for plagioclase, the positions of maxima diverge from a simple relationship to experimental geometry. Nonetheless, $(100)_{Cpx}$ poles are still rarer in orientations parallel to the spindle rotation axis, while $(001)_{Cpx}$ poles are still slightly more commonly oriented parallel to the rotation axis (Fig. 5f). The stronger clinopyroxene CPO in scan-0ϒ̇ (J_{ODF} = 1.23) is likely at least partly an artefact of the dramatically lower number of grains contributing to the CPO. The locations of the weak $(010)_{Cpx}$ and $(001)_{Cpx}$ maxima in scan-0ϒ̇ are identical to those of scan-Hϒ̇, and thus more clearly related to experimental geometry than the CPO of plagioclase in the same scan, although the location of the $(100)_{Cpx}$ maximum is rotated ~ 90° compared to that of scan-Hϒ̇ (Fig. 5i).

3.2.5 Fe-spinel CPO

The Fe-Spl CPO is essentially uniformly distributed, with texture index (J_{ODF}) not exceeding 1.01 in any of the three scans (Fig. S9). The extremely weak regularly spaced maxima visible in the pole figures are an artefact resulting from the skeletal habit of Fe-spinel

- single skeletal grains appear as multiple identically oriented crystals, artificially increasing the frequency of that orientation in the ODF (Fig. S9).

3.3 Crystal size distribution and kinetics

We produced CSD plots for each phase in each scan area (Fig. 5 and Fig. 6). Pl CSDs are always curved with a concave-up pattern. In addition, scans -Lϓ̇ and -0ϓ̇ also show a downturn at low crystal sizes (Fig. 6a,b). The concave-upward curvature is observed only in Pl (Fig. 5a,d,g and Fig. 6a,b) and allows interpolation of Pl CSD curves using two straight lines (Fig. 6a): a steeper one at smaller crystal sizes and a gentler one at larger sizes. Cpx shows a very steep CSD interpolation line in scan-Hϓ̇, but its slope gradually decreases in scans -Lϓ̇ and -0ϓ̇ (Fig. 6c,d). Cpx CSDs present a downturn at low crystal sizes, except for scan-0ϓ̇ where the CSD appears to be more linear (Fig. 6c,d). Finally, Fe-Spl shows a linear CSD in scan-Hϓ̇, a small hump downwards pattern with a spike up at smallest crystal size in scan-Lϓ̇ and a downturn at low crystal sizes in scan-0ϓ̇ (Fig. 6e,f).

3.3.1 Crystal Number Density, Nucleation and growth rates

The crystal number density (N_A), average nucleation rate (J_M) and maximum growth rate (G_{MAX}) estimates for each mineral phase within each scan are shown in Table 2. It is important to point out that these are estimates of the apparent J and G. J and G do not remain constant over time or with respect to crystal size during the experiment. Consequently, in this work, J_M and G_{MAX} are time-integrated values used as proxies to understand the relative effect of ϓ̇ on J and G, but their estimated absolute values do not represent actual values achieved during the experiment at specific times. The Pl G_{MAX} increases from scan-Hϓ̇ (1.57×10^{-10} ms^{-1}) to scan-Lϓ̇ (2.18×10^{-10} ms^{-1}) but shows the lowest value in scan-0ϓ̇ (1.08×10^{-10} ms^{-1}), while the Pl J_M smoothly decreases from the highest to the lowest inferred ϓ̇ area, from 2.7×10^{6} to

1.7×10^{6} m^{-3}s^{-1}. Pl N_A decreases with decreasing inferred $\dot{\Upsilon}$ from 4.4×10^{-8} to 2.16×10^{-8} m^{-2}. The Cpx G_{MAX} increases with decreasing inferred $\dot{\Upsilon}$, from 5.6×10^{-11} to 1.29×10^{-10} ms^{-1}, while J_M shows a opposite trend, decreasing from 1.3×10^{8} to 1.98×10^{7} m^{-3}s^{-1}. Cpx N_A likewise decreases with decreasing inferred $\dot{\Upsilon}$ from 5.48×10^{-8} to 1.84×10^{-8} m^{-2}. Finally, Fe-Spl G_{MAX} increases from scan-H$\dot{\Upsilon}$ (5.5×10^{-11} ms^{-1}) to scan-L$\dot{\Upsilon}$ (6.6×10^{-11} ms^{-1}), but like Pl is again lower in scan-0$\dot{\Upsilon}$ (5.1×10^{-11} ms^{-1}). Fe-Spl J_M shows quite similar values among the three scans ranging from 2.88×10^{7} m^{-3}s^{-1} to 2.83×10^{7} m^{-3}s^{-1}. Fe-Spl N_A also varies only slightly, between 1.26×10^{-8} and 1.41×10^{-8} m^{-2}.

3.4 Glass composition

Glass compositions were acquired for the two samples of the Md run (sections s28106 and s28107, 10 and 20 mm below the surface, respectively). Results of the glass analysis (for MgO, Al_2O_3 and SiO_2) for both samples are shown in Figure 7.

In general, Md-s28107 exhibits minor to moderate chemical variations in major elements, depending on the specific element considered. For example, MgO ranges from 4.45 to 5.01 wt.%, Al_2O_3 from 14.98 to 16.17 wt.%, and SiO_2 from 51.28 to 54.32 wt.% (Fig. 7a, b). The analysis of glass composition in Md-s28106, collected approximately 10 mm above Md-s28107, allowed us to quantify chemical variability along the vertical axis, thereby providing a more complete picture of the compositional heterogeneity generated in the experimental sample. When considering the overall chemical variation, the glass appears significantly more heterogeneous than suggested by any single sample. MgO content varies from a minimum of about 3.51 wt.% to a maximum of about 5.1 wt.% (Fig. 7). Al_2O_3 and SiO_2 chemical variation span from 14.98 wt.% to 17.17 wt.% and from 51.28 wt.% to 55.77 wt.%, respectively. Most of the major oxides analysed show a variability of their glass concentration between 1.5 wt.%

and 4.49 wt.%, which translates into a relative variation per individual oxide ranging from 8.4% to 43.2%.

3.5 Cluster chemistry

Following the cluster validation (Appendix 1), we defined the number of unique chemical clusters for each mineral phase. Fig. S10 reports the cluster validation procedure and the clustering results for Cpx. In detail, clustering analysis underlines the presence of three, three, and two distinct clusters for Pl, Cpx, and Fe-Spl (Fig. 8), respectively. In the following sub-sections, we briefly summarise the main chemical characteristics of the identified clusters.

3.5.1 Pl clusters

Cluster analysis shows that Pl data group into three clusters (CLp1, CLp2, and CLp3; Fig. 8a), CLp1 is always found in the overgrowth dark rims, CLp2 in the portion filling the core hollows of the skeletal structure and CLp3 in the main skeletal cores (Fig. S11). The clusters' chemical compositions are:

(i) CLp1 presents an Anorthite content = An_{62} (Fig. S12a, Tab. 3) and features the lowest FeO content (median (M) = 1.76 wt.%) and K_2O (M = 0.55 wt.%), median compositions for all the major elements can be found in table 3 or visualised in fig. 8a.

(ii, iii) CLp2 (An_{67}) and CLp3 (An_{68}) show an almost identical composition for all oxides except for FeO, which is higher in CLp3 ($M = 2.61 \pm 0.05$ wt.%) than in CLp2 ($M = 2.09 \pm 0.05$ wt.%). The median oxide K_2O contents are M = 0.39 wt.% for both clusters. For the subsequent discussion, we decided to combine CLp2 and CLp3 into a single cluster (Clp2+3, Fig. S11). This choice was made after two considerations: (i) the two clusters present an almost identical composition except for the higher FeO content in CLp3. (ii) The cluster CLp2 is only found in the areas infilling the hollow-textured skeletal cores, such areas, depending on the cut, are often very tiny (< 2 µm, especially for microlites) and thus hard to resolve, contributing to the noisy distribution of CLp2 (Fig. S11).

3.5.2 Cpx clusters

Cpx exhibits three chemically distinct clusters (CLc1, CLc2, and CLc3; Fig. 8b). CLc1 is mainly found in the dark core, CLc2 in the bright irregular mantle, and CLc3 in the rim (Figs. 9a and S10b). Their detailed chemical signatures are:

(i) CLc1 is the most mafic cluster (median Mg# = [Mg/(Mg+Fe)]*100) = 80.2), is augitic in composition with a Wollastonite = Wo_{42} (Fig. S12b, Tab. 3) and register a higher CaO/Al_2O_3 ratio. Of the three clusters Clc1 generally features the highest content of MgO (M = 16.06 wt.%) and SiO_2 (M = 49.34 wt.%) and the lowest content of Al_2O_3 (M = 4.68 wt.%), FeO (M = 7.13 wt.%) and TiO_2 (M = 1.17 wt.%). The CaO content varies significantly within the cluster but is lower compared with other clusters.

(ii) CL2c is diopsidic in composition (Wo_{46}) and displays lower Mg# (M = 71.9) and CaO/Al_2O_3 values with respect to the other clusters. The cluster features the highest Al_2O_3 (M = 7.58 wt.%), FeO (M = 9.15 wt.%) and TiO_2 (M = 2.21 wt.%) values and the lowest SiO_2 (M = 44.99 wt.%) and MgO (M = 13.10 wt.%) values among the three clusters. The CaO content of CLc2 is very similar to that of CLc3 (M = 21.44 wt.%).

(iii) CLc3 (Wo_{45}) features medium to high Mg# and CaO/Al_2O_3 partially overlapping with the ranges occupied by CLc1 (Fig. 8b) but showing a lower median Mg# (M = 77.2) and CaO/Al_2O_3 values than CLc1. The concentration of all the analysed oxides is generally in between CLc1 and CLc2 concentrations, with the following median values: SiO_2 (M = 47.83 wt.%), Al_2O_3 (M = 5.86 wt.%), TiO_2 (M = 1.54 wt.%), MgO (M = 14.57 wt.%), FeO (M = 7.71 wt.%), CaO (M = 21.42 wt.%).

3.5.3 Spl clusters

Fe-Spl shows no zonation but two main compositional clusters (CLs1 and CLs2; Fig. 8c). The majority of Fe-Spl show a CLs1 composition, while very rare single crystals, usually attached to bigger CLs1 crystals, exhibit a CLs2 composition. This rare phase has been detected only very close to the spindle in sample Md-s28106. The clusters' compositions are:

(i) CLs1 present a high Magnesioferrite component = Mfr_{53} (Fig. S12c, Tab. 3) and minor Magnetite (Mt_{44}) and Ulvöspinel (Usp_{3}). CLs1 has a significantly higher Al_2O_3 (M = 7.90 wt.%), MnO (M = 0.53 wt.%) and MgO (M = 11.90 wt.%) content compared with CLs2 and a slightly higher SiO_2 content (M = 0.13 wt.%), while TiO_2 content is much lower (M = 4.20 wt.%) compared with CLs2 (M = 14.62 wt.%) and median FeO is just slightly lower (M_{CLs1} = 69.56 wt.%; M_{CLs2} = 69.97).

(ii) CLs2 (Mt_{60}), present a higher Ulvöspinel component (Usp_{23}). It shows a median TiO_2 of 14.62 wt.%, and a lower amount of Al_2O_3 (M = 1.88 wt.%) and MgO (M = 5.49 wt.%) compared with CLs1. The contents of other oxides in CLs2 are: SiO_2 (M = 0.08 wt.%), FeO (M = 69.97 wt.%) and MnO (M = 0.25 wt.%).

3.6 Distribution of chemical clusters in different strain zones

RF classification, applied on EPMA chemical maps, defines three 2D clustered maps (one for each strain area; Figure 9).

3.6.1 Spatial distribution of Pl chemical clusters

While changes in the area fraction of different chemical clusters can be compared across maps for Cpx and Fe-Spl, doing so for Pl may be misleading and should be avoided. Pl crystals show a stronger preferred orientation, and in scan-Hϓ̇ they are mostly sectioned similarly, whereas in scan-Lϓ̇ a large, differently oriented crystal dominates the map. This may artificially alter the apparent proportions of chemical zones, introducing bias in the comparison. The area percentage of CLp1 (associated with Pl rims, An_{62}) decreases with decreasing inferred relative $\dot{\gamma}$ from scan-H$\dot{\gamma}$ (70.5%) to scan-L$\dot{\gamma}$ (41%) but increases again in scan-0$\dot{\gamma}$ to 66.4% (Fig. 9).

3.6.2 Spatial distribution of Cpx chemical clusters

The distribution of the three Cpx clusters shows a clear relationship to the inferred relative $\dot{\gamma}$ (Fig. 9). CLc1 ($Wo_{42.6}$) area percentage increases with decreasing inferred $\dot{\gamma}$, from 4.9% in scan-H$\dot{\gamma}$, through 11.75% in scan-L$\dot{\gamma}$, up to 21.41% in scan-0$\dot{\gamma}$. A similar trend is observed in CLc2 ($Wo_{45.8}$) which in scan-H$\dot{\gamma}$ shows an area percentage of 20.9%, in scan-L$\dot{\gamma}$ of 26.75%, and in scan-0$\dot{\gamma}$ of 33.9%. In contrast, CLp3 ($Wo_{44.9}$) decreases with decreasing $\dot{\gamma}$ (74.3% in scan-H$\dot{\gamma}$, 61.5% in scan-0$\dot{\gamma}$, and 44.7% in scan-0$\dot{\gamma}$). To summarize, Cpx core and bright mantle clusters (CLc1 and CLc2) become more abundant with decreasing strain rate, while the rim cluster (CLp3) decreases in abundance. We note that, while it was always possible to segment CLc2 and CLc3, some challenge was encountered in accurately quantifying the area percentage of CLc1 in scan-H$\dot{\gamma}$.

3.6.3 Spatial distribution of Fe-Spl chemical clusters

Fe-Spl are mostly classified as CLs1 in s28107 in all samples. BSE image analysis highlights the presence of a texturally distinguished phase (then chemically recognized as CLs2) only in the area close to the spindle of s28106 (supplementary Fig. S13).

4 DISCUSSION

4.1 Crystallisation kinetics

To reconstruct crystallization kinetics in our experimental set-up, we first modelled the crystallization sequence using MELTS (Gualda et al., 2012). Under our experimental conditions, MELTS predicts the formation of the same mineral assemblage observed in the experiments (Pl, Cpx, and Fe-Spl), with liquidus temperatures of 1259°C for Fe-Spl and 1193°C for both Pl and Cpx.

Previous experiments on similar starting compositions (Mt. Etna trachybasalts) and under comparable conditions (atmospheric pressure, temperatures between 1182°C and 1131°C, and imposed deformation using a concentric cylinder apparatus; Vona et al., 2011; Vona and Romano, 2013; Vetere et al., 2024; Mollo et al., 2024) showed that Pl crystallized at higher temperatures than Cpx. Specifically, in the experiments performed by Vona et al. (2011) and Mollo et al. (2024), Pl crystallized at 1182°C and 1170°C respectively, while Cpx appeared only around 1131°C (Vona et al., 2011). In contrast, in our experiments, as confirmed by the snapshot runs, all three phases crystallized only during the lower-temperature step (Sd2) at 1130°C. We attribute the absence of Fe-Spl and Pl during the first hour at 1170°C (experiment Sd3) to the initial nucleation delay (i.e., incubation time). In the Vona et al. (2011) experiments, the melt was held at the dwell temperature (1182.4°C) for significantly longer time intervals (>> 8h), while in Mollo et al. (2024) a constant T of 1170°C was kept for 72h. This suggest that, under our experimental conditions, one hour at 1170°C is not sufficient to initiate nucleation, despite being below the liquidus. Crystal nucleation can be delayed at lower degrees of undercooling (Lofgren, 2014), and incubation time can also be increased by superheating treatments (Lofgren, 2014; First *et al.,* 2020; Rusiecka *et al.*, 2020), which may explain the delayed crystallization we observed. Finally, the crystallization of Fe-Spl alone after one hour at 1130°C in static conditions (Ss1), compared to the crystallization of all phases at the same temperature under dynamic conditions, highlights the role of deformation in reducing incubation time and promoting crystal nucleation (Kouchi *et al.*, 1983).

4.1.1 Pl crystallisation

All Pl CSDs display a concave-up curvature (Figs. 5 and 6a), suggesting the presence of two Pl populations characterized by distinct nucleation and growth regimes. To better characterize these regimes, we applied separate linear regressions to the data points before and after the inflection point in the CSD curve (Fig. 6a,b). The population consisting of larger Pl crystals (L > 100 µm) displays a gentler CSD slope and lower intercept, indicative of lower nucleation rate and higher average growth rates. This population is interpreted to have formed earliest in the experiment (“first nucleation pulse”) and have experienced a longer growth history. We note that Pl from the Sd2 run lacks dark overgrowth rims. This, combined with further chemical analysis of Pl from this run, indicates that only CLp2–3 compositions were present during the early stages of crystallisation (Fig. S14a).

In contrast, the population of smaller Pl crystals (L < 100 µm), is characterized by a steep CSD slope and a high intercept, features consistent with a high nucleation rate and relatively lower average growth rates. This population presents a Clp1 composition, the same recorded in the outer (henceforth “overgrowth”) rims of larger Pl. We infer that these smaller crystals mainly formed during the final step at 1150 °C, together with the overgrowth rims. The presence of large euhedral portions of the smaller crystals with CLp1 composition (Fig. 9) indeed excludes the possibility that all of them crystallized during rapid quenching, which would be expected to result in plagioclase of a different composition to any grown during the main experiment. However, we cannot completely rule out that some of the smaller, acicular crystals may have formed during quenching, due to the difficulty of obtaining chemical information for these crystals.

We focus the following discussion on the first nucleation pulse only, which we assume to have occurred during the first step at 1130°C (as also confirmed by exp. Sd2), because we are mainly interested in unveiling the impact that early J and G events played in the evolution of the system at varying ϒ̇.

In addition to the concave-up curvature, Pl CSDs in scan-0ϓ̇ and scan-Lϓ̇ also show a downturn at low crystal sizes (Fig. 6a,b). This pattern is often related to coarsening (Cashman and Ferry, 1988; Higgins, 1999, 2002, 2011; Mills and Glazner, 2013), a process which promotes the growth of crystals larger than a critical threshold size over smaller crystals (Higgins, 2011), and which has been shown to be particularly favoured under oscillating temperature conditions, as in the case of the present study (Mills and Glazner, 2013). While in scan-0ϓ̇ the down-turn at smaller crystal sizes can be confidently attributed to coarsening effects, given that the minimum (3D) crystal size class in the CSD (11.4 µm) is well above the minimum detected grain size with EBSD map (2 pixels, thus ~4.6 µm, Appendix 1), in scan-Lϓ̇ we cannot rule out a minor contribution from resolution limitations, since the minimum (3D) CSD size class is equal to the EBSD minimum detected grain size (again 2 pixels and ~4.6 µm, Appendix 1).

Many Pl phenocrysts present a Fe-rich skeletal core (CLp2+3 in composition), interpreted as fast growth features (Chernov, 1974; Kirkpatrick, 1975; Sunagawa, 1999) during the first low temperature step at 1130°C (Fig. 3b, Fig. 10). This is also confirmed by the snapshot experiments, in which skeletal BSE-bright plagioclase with small and sometimes hollow darker sectors only form at 1130°C (Sd2, Figs. 2 and S15), with both CLp2 and CLp3 compositions recorded in the Sd2 run product (Fig.S14a). Some of the skeletal cores in the Md show minor signs of resorption. This might indicate that during the 1170°C step, the growth rate was greatly reduced or completely inhibited, with possible minor resorption. While larger Pl skeletal cores were at most only slightly resorbed during the high temperature steps, the presence of coarsening features in CSDs for scan-0ϓ̇ and -Lϓ̇ (Fig. 6) suggests that smaller crystals, with higher surface energy to volume ratios, may have been successively and preferentially resorbed during the re-heating steps at 1170°C, promoting the growth of larger phenocrysts during oscillations at 1130°C (Fig. 10). The presence of some sector-zoned Pl in both Md and Sd2 indicates that the Fe-poor {100} sectors form in the first nucleation pulse, during the first step at 1130°C. The hollow sections of the skeletal cores and the sometimes-incomplete {100} sectors show signs of being filled at varying degrees. The infill is sometimes homogeneous and sometimes shows oscillatory zoning (CLp2 and CLp3; Fig. 3), this confirms that cycles of slight resorption and filling occurred at different degrees in Pl {100} sectors during temperature oscillation (Fig. 10). Finally, the Pl overgrowth rims have the same composition as the crystals assigned to the "second nucleation pulse" (microlites, CLp1) and thus we propose that they formed during the second pulse of nucleation occurring during the long dwell at 1150 degrees (Fig. 10).

4.1.2 Cpx crystallisation

As shown in Fig. 6, the Cpx CSD slope markedly decreases from the H$\dot{\Upsilon}$ to the 0$\dot{\Upsilon}$ domain, indicating an increase in growth rate with decreasing $\dot{\Upsilon}$. The intercept, which is proportional to the nucleation rate (Cashman and Marsh, 1988; Toramaru, 2022), shows the opposite trend, decreasing nucleation rate with decreasing $\dot{\Upsilon}$. These trends are consistent with the quantitative estimates of apparent G_{MAX} and J_M obtained using the approach of Hammer and Rutherford (2002; Table 1 and Fig. 11), which show that J_M in Scan-H$\dot{\Upsilon}$ is approximately an order of magnitude higher, while G_{MAX} is about an order of magnitude lower.

The CSD of Cpx shows no concave-up curvature (Fig. 6), which implies the presence of just one family of crystals, formed during the experiment. Scan-H$\dot{\Upsilon}$ shows a downturn at smaller crystal sizes (Fig. 6), which we rule out as a map resolution artifact, as it affects more than just the smallest size class and the minimum CSD length class lies above the minimum grain size threshold used for grain reconstruction (Appendix 1). A plausible explanation for this curvature is a coarsening effect. The fact that this is observed only in Scan-H$\dot{\Upsilon}$ is likely reflecting the distinct growth conditions near the spindle at higher initial strain rates. In scan-H$\dot{\Upsilon}$, the apparent J is approximately one order of magnitude higher than in the other areas, implying the formation of many small crystals during the first nucleation pulse. This evidence, combined with the presence of resorption textures (detailed below), suggests that during the subsequent temperature oscillations, numerous small crystals and nuclei were reabsorbed, thereby favouring the growth of larger ones. In contrast, the lower J and higher growth rates in other regions resulted in fewer, larger crystals already at the end of the first step at 1130°C, effectively inhibiting resorption-driven coarsening.

Cpx cores (CLc1) and bright mantles (CLc2) formed during the first step at 1130°C (Fig. 10). This is also confirmed by exp. Sd2, where both dark and bright areas are observed (Fig. S15). Targeted analyses of these areas within the Sd2 run confirm that both compositions (CLc1 and CLc2) are already present at early stages of crystallisation (Fig. S14b). CLc1 is the more mafic with higher Mg# and higher CaO/Al_2O_3 ratio, and it is always found in the cores showing only minor resorption. CLc2 has high values of Al_2O_3, $TiO_{2,}$ and shows also higher values of Na_2O (Tab. ST3).

The presence of both zones since the first nucleation pulse allows for several possible interpretations:

(i) Clc1 represents the initial composition, followed closely by the rapid growth of Clc2 bright mantles as disequilibrium zones. Indeed, high Cpx growth rates can produce compositional boundary layers enriched in incompatible elements such as Al, Na, and Ti, leading to the formation of Al-rich Cpx zones (Mollo *et al.*, 2010, 2013).

(ii) Alternatively, Clc1 and Clc2 may have formed simultaneously, with the dark cores and bright mantles corresponding to hourglass and prism sectors of sector-zoned crystals, respectively. Their compositions are also consistent with this interpretation, as Clc1 is enriched in MgO and SiO2, and Clc2 in Al2O3 and TiO2 (Ubide *et al.*, 2019).

(iii) A third possibility is that Clc2 formed first as a skeletal core, later partially filled by Clc1. Support for this may come from the control exp. Sd2, where darker crystal sectors appear only partially developed, suggesting incomplete filling.

Although none of these hypotheses can be entirely confirmed or ruled out, the frequent occurrence of incomplete dark sectors and the presence of sector-zoned crystals with Clc1 and Clc2 compositions support the latter two scenarios, which are not mutually exclusive. According to Welsch et al. (2016), sector zoning can result from the rapid growth of dendritic, Al-rich {-111} hourglass sectors, subsequently backfilled by Al-poor prismatic {hk0} sectors. In contrast, our observations suggest a reversed pattern, with Al-rich zones associated with prismatic sectors, consistent with the findings of Ubide et al. (2019) on clinopyroxenes. It is also possible that the two zones formed simultaneously, without any backfilling process, and that the incomplete fill simply reflects the skeletal or hopper habit of the crystals, which preserves cavities along {-111} faces. However, additional experiments are needed to better constrain the process behind sector zoning formation in our experimental conditions.

The irregular shape of the CLc2 bright mantles is interpreted as a clear resorption texture, inferring that Cpx was not stable at 1170°C. This further indicates that the mantle zone evolved during successive cycles of growth (at low dwell-T1 = 1130°C) and resorption (at high dwell-T2 = 1170°C), where the net growth rate was always larger than the net resorption rate allowing the bright mantle to be preserved. This process clearly led to the formation of oscillatory zoning in some areas of the sample, such as in Scan-0Ύ̇, where higher growth rates have been recorded and different Cpx show oscillatory zoning between the first, more homogeneous bright mantle layer and the final overgrowth rim (Fig. 3c). We infer that this feature is preserved only in scan-0Ύ̇ because of the competition between resorption (at 1170°C) and growth (at 1130°C). The much higher G_{MAX} in Scan-0Ύ̇ might allowed the oscillatory zonation to be preserved in this region. The last resorption cycle occurred during the final step at 1170°C before lowering the temperature to dwell-T3 (1150°C) for 48 hours (Fig. 10). During the 48-hour step at dwell-T3 we have the formation of the last rim (Fig. 10). The lack of a concave-up curvature in CSD, coupled with the lack of microlites showing clear quenching habits, and the evidence that even the smallest Cpx show the three different zones (core, mantle and final rim), allow us to confidently attribute the rim growth to the last phase at dwell-T3 rather than quenching (Fig. 10).

4.1.3 Fe-Spl crystallisation

Fe-Spl CSD curves are quite linear (Fig. 6), and their chemical composition is mostly homogeneous within the sample and show no evidence of zoning, with CLs1 composition dominating all the analysed areas. The absence of clear signals of two populations in the CSD, suggest this phase crystallize during a single nucleation pulse, occurred during the first step at 1130°C (Fig. 10) as also confirmed by exp. Sd2.

4.2 The impact of strain rate on nucleation, growth rates

Pl presents the highest crystal number density in scan-HΎ̇, reflected also in the highest values of nucleation rate (Fig. 4 and Fig. 12). Since scan-HΎ̇ is the area characterized by the highest inferred Ύ̇, this suggests a direct relationship between nucleation rate and Ύ̇ (Table 2). This agrees with the results reported in Mollo et al. (2024), that highlight higher Pl fraction and higher nucleation rate at increasing Ύ̇. In our experiments, this effect is even more pronounced for Cpx, where the nucleation rate increases by an order of magnitude from inferred lowest to highest Ύ̇ domains, whereas measured G of Cpx in our experiments shows the inverse trend, decreasing with increasing $\dot{\gamma}$ (Fig. 11a). Scan-0$\dot{\gamma}$ shows less evidence of deformation compared to scans H$\dot{\gamma}$ and L$\dot{\gamma}$. Following the trend of G variation with $\dot{\gamma}$ for Cpx (Fig. 11a), we would also expect Pl to show the maximum value of G in this zone. Indeed, Mollo et al. (2024) crystallised Pl under almost identical conditions (same starting composition, P = 1 atm, T = 1170°C, $\dot{\gamma}$ = 0, 0.1, 1 and 10 s^{-1}) and found that average G decreases at increasing $\dot{\gamma}$. However, this was not the case in our experiments (Fig. 11), where the smallest Pl G was recorded in scan-0$\dot{\gamma}$. We interpret the Pl discrepancy in the growth rate trend for the lowest inferred $\dot{\gamma}$ domain to be modulated by the competition with Cpx for nutrients (Meth and Carlson, 2005; Nabelek *et al.*, 2010; Shea and Hammer, 2013). More specifically, by "competition" we refer to the effect produced by the higher growth rate of a specific phase (e.g. Cpx), which locally modifies the residual melt composition, thereby influencing the nucleation and growth rates of the other phases (e.g., Pl). A higher growth rate of Cpx might accelerate local melt depletion of competing mineral phase components and quickly reduce the degree of undercooling of the melt and thus the driving force for further crystallisation. As a consequence, the growth of competing phases such as Pl can be inhibited. Similar effects have been already reported in relation to crystallisation dynamics in magmatic systems (Brandeis and Jaupart, 1986; Hammer and Rutherford, 2002; Mangler *et al.*, 2022). It is important to stress that Pl growth rate suppression by competition with Cpx in these experiments requires Ca to be the limiting element for Pl growth – crystallisation of the measured Cpx compositions should deplete the melt of CaO but enrich it in Al_2O_3.

To better understand how the dynamics of initial nucleation influenced the growth of the crystalline phases, it is important to identify which phase crystallised first. MELTS estimates suggest that at equilibrium, the first phase to form would be Fe-Spl, followed by contemporaneous formation of Pl and Cpx at the same temperature conditions. However, experimental studies at comparable conditions (e.g., Vona *et al.*, 2011; Vona and Romano, 2013; Arzilli *et al.*, 2019; Vetere *et al.*, 2024) report lower liquidus temperatures for Cpx, which typically appears after Pl. For example, Vona et al. (2011) observed Pl starting to crystallize at 1182.4 °C, while Cpx was first detected only at 1131 °C. At comparable conditions, Vetere et al. (2024) observed the crystallization of both Pl and Cpx at 1150 °C, with Pl consistently more abundant than Cpx, regardless of the dwell time (3, 6, or 9 h). In our case, determining the relative timing of Pl and Cpx nucleation is challenging. Arzilli et al. (2019) observed dendritic Cpx growing heterogeneously on Pl, but no evidence of such growth is found in our samples. We therefore infer that Pl and Cpx crystallised either simultaneously or in close succession.

The fact that in our experiments only Cpx presents the expected monotonous increase in J and decrease in G with increasing $\dot{\Upsilon}$, the same trend observed for Pl crystallising alone in melt under strain by Mollo et al. (2024), might suggest that Cpx nucleated slightly earlier compared to Pl, modulating the nucleation and growth behaviour of the latter phase. Even if we assume that Cpx nucleated slightly later, its marked spatial variability in nucleation and growth rates, spanning approximately one order of magnitude, compared to the relatively minor variation observed for Pl, likely still governed the growth dynamics of Pl and influenced the final phase proportions.

All these observations highlight how variations in $\dot{\Upsilon}$ can impact nucleation rates and, in turn, influence the final mineral phase proportion, and magma rheology, generating local textural and melt chemistry variations. The increase in nucleation rate with increasing deformation can directly impact the rheology of rising magmas, contributing, along with other conduit processes, to modulate variations in eruptive style. The effect of deformation on the reduction of incubation time and the increase in nucleation rate has been extensively studied in the literature, and our experimental results confirm the relationship already observed by other authors (Kouchi *et al.*, 1983; Vona *et al.*, 2011; Vona and Romano, 2013; Chevrel *et al.*, 2015; Tripoli *et al.*, 2019; Di Fiore *et al.*, 2021, 2022, 2023; Vetere *et al.*, 2021, 2024; Mollo *et al.*, 2024). This effect can be attributed to different processes. Considering theoretical nucleation under steady-state conditions, the nucleation rate can be calculated using the following equation (Toschev, 1973; Kouchi et al., 1986):

$$\mathrm{J} = \mathrm{KD}^{*}\exp\left(\frac{-\Delta \mathrm{G}^{*}}{\mathrm{kT}}\right) \tag{6}$$

where K is a constant, D* is the diffusional transport factor, ΔG* is the activation energy (i.e., the minimum energy required by the system to generate stable crystal nuclei), T is the temperature, and k is the Boltzmann constant. In this context, deformation can promote nucleation by primarily affecting both the diffusional transport factor (D*) and the activation energy (ΔG*). Specifically, deformation can enhance the convective transport of material, leading to an increase in D* (Kouchi et al., 1986; Vona and Romano, 2013; Vetere et al., 2024), and it can also provide mechanical energy that helps the system overcome the minimum ΔG* threshold required for the formation of the first nuclei (Tripoli et al., 2019).

4.3 The strain rate control on mineral proportion and residual melt composition

While, as discussed above, the relationship between deformation and nucleation is already established in the literature, our experimental results offer new insights into how the effect of $\dot{\Upsilon}$ on nucleation also influences the subsequent evolution of the system, modulating the mineral phase fraction, the development of specific textures, and the final composition of the residual glass. Mineral and chemical cluster proportions vary in space within the experiment, impacting the residual melt composition (Fig. 7), CSDs (Fig. 6) and magma rheology.

In two of the three scans, application of the Vona et al (2011) model yielded infinite viscosities, indicating crystallinities exceeding the maximum packing fraction (ϕ_{MAX}). This is unsurprising, given that growth proceeded after the cessation of spindle rotation. To investigate rheological variations despite this limitation, we adopted two alternative approaches: (1)

applying the Einstein-Roscoe equation with spherical crystals and $\phi_{MAX} = 0.6$; (2) forcing the Vona model by setting ϕ_{MAX} slightly higher than the observed maximum crystallinity ($\phi_{MAX} = 0.52$). Using the Einstein-Roscoe method, viscosity increases by roughly one order of magnitude with inferred $\dot{\gamma}$, from 5.63×10^4 Pa·s (scan-0$\dot{\gamma}$) to 3.34×10^5 Pa·s (scan-H$\dot{\gamma}$). When forcing the Vona model, the increase spans four orders of magnitude, from 9.28×10^4 Pa·s (scan-0$\dot{\gamma}$) to 6.10×10^8 Pa·s (scan-H$\dot{\gamma}$).

Although these values are approximations (neglecting strain localization, crystal orientation, and dynamic crystallinity evolution) they highlight two key insights: (1) the textural differences produced at varying $\dot{\gamma}$ can lead to viscosity contrasts of several orders of magnitude; (2) under our experimental conditions, ϕ_{MAX} was reached rapidly in all regions, implying no significant crystal migration occurred during the run. However, this does not preclude possible melt redistribution among different areas throughout the experiment.

In general, even considering glass re-equilibration and homogenization processes during 48 hours at a constant 1150°C, the glass composition varies significantly within the experiment. Notably, while significant variations in the residual glass composition can be observed globally in the sample, within the individual samples analysed (Md-s28106 and Md-s28107) this variation is only minor to moderate (Fig. 7). The main difference between the two samples is the depth at which they were cut in the drilled core (~ 10 mm for s28106 and ~ 20 mm for s28107, Fig. S2). This means that s28107 is also sampled closest to the hot-spot centre of the oven, and it might have experienced slightly higher temperatures compared to s28106. However, as the temperature gradient estimated using multiple thermocouples does not suggest large vertical variations in temperature (± 3°C) during the experiment, we rather associate the differences in residual glass composition to the presence of varying crystallinity within the sample. Indeed, a comparison between the crystal texture of the two samples close to the spindle reveal an even higher crystallinity in sample Md-s28106 (up to 57.7 area % of crystals, Fig.

S16), possibly responsible for the more evolved compositions of the residual glass recorded in this sample. This suggests heterogeneities in the degree of strain localisation in different portions of the whole experimental sample, with the possible formation of areas at higher and lower $\dot{\Upsilon}$ compared to the range observed in Md-s28107 only.

The variations in crystallinity and mineral assemblage suggest that different mineral phase proportions (in areas with varying $\dot{\Upsilon}$) may be the primary cause of the observed differences in residual glass composition. However, in our experimental samples, the real impact of the mineral assemblage on the measured glass composition might be masked by melt re-equilibration during the final step of the experimental run.

To estimate the true effect of different mineral phase proportions on residual glass composition, we calculate the ideal residual glass composition with a mass balance based on mineral phase and compositional cluster proportions for the different $\dot{\Upsilon}$ domains. In detail, we can use the phase proportions in different areas to recalculate the expected residual melt chemistry as follow:

$$C_{\mathrm{ResMelt}}^{\mathrm{ox}} = \frac{C_{\mathrm{StartMelt}}^{\mathrm{ox}} - C_{\mathrm{Cpx}}^{\mathrm{ox}} \cdot m_{\mathrm{Cpx}} - C_{\mathrm{plg}}^{\mathrm{ox}} \cdot m_{\mathrm{plg}} - C_{\mathrm{Fe-spl}}^{\mathrm{ox}} \cdot m_{\mathrm{Fe-spl}}}{m_{\mathrm{ResMelt}}};\ \ m_{\mathrm{phase}} = X_{\mathrm{phase}} \cdot \rho_{\mathrm{phase}} \qquad (7)$$

Where C is the wt.% concentration of the oxide (ox) in the respective phase (e.g., Cpx, Pl, etc.), m, X and, ρ are the mass, volume fraction and density of the respective phase. To calculate X, we assume that the crystal area fractions are equal to the crystal volume fractions (Brugger and Hammer, 2010). ResMelt is the residual melt and StartMelt is the glass starting composition before crystallisation. Being that the ρ of the residual melt it is not known a priori, the mass of the residual melt has been calculated iteratively till convergence has been reached. For each mineral phase, $C_{\mathrm{cryst}}^{\mathrm{ox}}$ and m have been estimated as the sum of each cluster mean composition and its relative volume fraction (X), as:

$$C_{\mathrm{cryst}}^{\mathrm{ox}} = \sum_{i=1}^{N} C_{\mathrm{cryst-CL_i}}^{\mathrm{ox}} \cdot m_{\mathrm{cryst-CL_i}}^{\mathrm{ox}} \qquad (8)$$

Where CL_i is the cluster number (from i to N). The residual glass mass balanced calculations are available in the supplementary table ST4. The composition of the residual glass thus calculated shows a more evolved range than that measured in sample Md-s28107 and is closer to that of sample s28106, with a minimum MgO content of 3.6 wt.% and a maximum SiO_2 content of 53.69 wt.%.

We observe that even the small variation in $\dot{\Upsilon}$ inferred to separate scan-0$\dot{\Upsilon}$ and scan-L$\dot{\Upsilon}$ can lead to strong differences in nucleation, growth, and competition between different mineralogical phases. This leads to variation in mineral phase proportions that can locally affect the residual melt composition, as shown by the variations in calculated residual melt chemistry for the areas of differing strain rates. The variation of residual melt composition (from s28106 to s28107) along the vertical of the sample is therefore inferred to be related to the complex nature of strain localisation within the sample. While this is sub ideal for experiments, these conditions are close to those of volcanic plumbing systems and lava flows at the surface.

As shown in section 3.2 and displayed in Figure 12a, at increasing relative $\dot{\Upsilon}$ we observe an increase in Pl fraction. If we observe the residual glass composition (estimated through eq.7 and eq.8) as a function of the variation in the Pl/Cpx fraction (Fig. 12b) we can observe that at increasing Pl/Cpx fraction, we have an increase in Mg#. This result helps us to quantify the potential nature and magnitude of chemical variation in residual glass due to variations in mineral proportions, which may be governed by variations in the $\dot{\Upsilon}$ to which crystallising magmas are subjected.

4.4 Strain rate control on chemical and textural evolution in natural systems

Magmatic systems exhibit complex chemical and physical variability in space and time, with strong to moderate thermal gradients and $\dot{\Upsilon}$ ranging from ~70 s^{-1} to 10^{-9} s^{-1} (Nicolas and Ildefonse, 1996; Papale, 1999; Piombo and Dragoni, 2009; Cashman *et al.*, 2013, 2017;

Caricchi and Blundy, 2015; Kolzenburg *et al.*, 2018a, 2018b). In this work, we observed how small variations in $\dot{\Upsilon}$ ($< 1s^{-1}$) can heavily influence nucleation and growth dynamics, exerting primary control on magma evolution.

Musu et. al. (2023) measured variations of the chemical composition of crystals and glass during the February-April 2021 eruptive sequence of Mt. Etna. The natural glass chemical variations were previously linked to input of varying proportions of new, more mafic magma throughout the eruptive series (Corsaro and Miraglia, 2022; Mollo *et al.*, 2022; Musu *et al.*, 2023). On the other hand, the discharge rate varied significantly during the lava fountaining sequence (Calvari and Nunnari, 2022). For example, the Feb 28 event presents a higher discharge rate, which might be associated with higher mean $\dot{\Upsilon}$ to which the erupted magma is subjected (Kolzenburg *et al.*, 2018a). The question we pose here is: how much of the chemical variation observed in the glass erupted at Etna is due to (1) different proportions of mafic magma involved vs (2) conduit dynamics ($\dot{\Upsilon}$ variations)?

Assuming that the starting melt that drove the 2021 Etna eruption and the melt used in our experiments have a similar composition, we used our experimental results as a guide to interpret the chemical variations observed during the Etna Feb-Apr 2021 eruptive sequence. It is crucial to note that the experiments are conducted under different starting conditions than those found in the natural environment of Mt. Etna (e.g., H_2O content, fO_2, and pressures). The upcoming comparison primarily aims to highlight the potential impact of the $\dot{\Upsilon}$ on residual melt composition, assuming all other conditions remain constant.

The plots in Figure 13 directly compare the total degree of chemical variation observed throughout our experiment (right side of the plots) with that recorded at Mt. Etna during the February–April 2021 eruptive sequence. As shown in Figure 13 (see also Musu et al., 2023), the chemical variability observed in our experiments falls within the same compositional range as that recorded at Mt. Etna during the February–April 2021 eruptive sequence. This underscores the possibility that $\dot{\gamma}$ alone could drive glass chemical variations of a magnitude sufficient to explain the natural variability observed at Mt. Etna.

From the estimated residual melt composition in our experiments, we observe an increase in MgO content at higher $\dot{\gamma}$. As can be observed in Fig. 13, the 28 Feb event, characterised by a higher total average discharge rate (Calvari and Nunnari, 2022; Musu *et al.*, 2023), presents a chemical composition consistent with what we would expect for higher $\dot{\gamma}$ values, based on our experimental observations (e.g., with an increase in MgO content – Fig. 12a). In our experiment, glass chemical variations are directly related to variations in mineral phase proportion (with higher Pl fraction at higher $\dot{\gamma}$; Fig. 12a). The 28 Feb eruption is also the one that shows a higher amount of Pl microlites in the erupted products (Musu et al., 2023).

In light of these results, our question is: could the different and more mafic composition of the 28 Feb (Corsaro and Miraglia, 2022; Musu *et al.*, 2023) event be due to higher ascent velocities and thus higher $\dot{\gamma}$ experienced by the magma? Our experimental results suggest that this might be possible, but obviously, whether the impact of the $\dot{\gamma}$ on the glass composition at Etna can be exactly described by the pattern observed in our experiments at present remains speculative.

5 CONCLUSIONS

We reported on the effect of shear strain rate ($\dot{\gamma}$) on the textural and chemical evolution of basaltic melt. We observe that, at the same temperature, an increase in $\dot{\gamma}$ results in higher nucleation rates and thus influences the competition for nutrients in different mineral phases that are forming in the crystallising melt. The impact of $\dot{\gamma}$ variation on initial crystal number density can lead to significant variations in the final mineral phase proportion and thus in the composition of residual glasses. These results underline the role of $\dot{\gamma}$ in textural and chemical changes of erupted products, a role that cannot be overlooked if we want to correctly link variations in chemical and textural signals to deep magmatic processes or emplacement dynamics. Future detailed investigation is required to isolate the contribution of $\dot{\Upsilon}$ to chemical and textural variations from that of other magmatic processes at Mt. Etna and, more generally, in active natural systems.

ACKNOWLEDGMENT

The authors acknowledge Dr. Florence Bégué (University of Geneva) and Dr. Martin Robyr (University of Lausanne) for their valuable assistance with the collection and quality control of EPMA analyses. We also thank Jean-Marie Boccard (University of Geneva) and Ilka Wünsche (Department of Lithospheric Research, University of Vienna) for their important contributions to sample preparation. Finally, we gratefully acknowledge Prof. Daniele Morgavi (University of Naples Federico II, Naples) for his important contribution to the realisation and fine-tuning of the control experiments.

FUNDING

This research was supported by the SWISS NATIONAL SCIENCE FOUNDATION (grant n. 200021_184632).

DATA AVALAIBILITY STATEMENT

The data underlying this article are available in the article and in its online supplementary material. New geochemical data are also available in the repository EarthChem (https://doi.org/10.60520/IEDA/113368).

CONFLICT OF INTEREST

The authors declare that they have no conflicts of interest.

REFERENCES

Abbott, P. M., Plunkett, G., Corona, C., Chellman, N. J., McConnell, J. R., Pilcher, J. R., Stoffel, M. & Sigl, M. (2021). Cryptotephra from the Icelandic Veiðivötn 1477 CE eruption in a Greenland ice core: confirming the dating of volcanic events in the 1450s CE and assessing the eruption's climatic impact. *Climate of the Past*. Copernicus GmbH **17**, 565–585.

Albert, H., Larrea, P., Costa, F., Widom, E. & Siebe, C. (2020). Crystals reveal magma convection and melt transport in dyke-fed eruptions. *Scientific Reports*. Nature Publishing Group **10**, 11632.

Andronico, D. *et al.* (2005). A multi-disciplinary study of the 2002–03 Etna eruption: insights into a complex plumbing system. *Bulletin of Volcanology*. Springer **67**, 314–330.

Armienti, P. (2008). Decryption of igneous rock textures: crystal size distribution tools. *Reviews in Mineralogy and Geochemistry*. Mineralogical Society of America **69**, 623–649.

Arzilli, F. *et al.* (2019). Magma fragmentation in highly explosive basaltic eruptions induced by rapid crystallization. *Nature Geoscience*. Nature Publishing Group **12**, 1023–1028.

Baker, D. R., Brun, F., O'shaughnessy, C., Mancini, L., Fife, J. L. & Rivers, M. (2012). A four-dimensional X-ray tomographic microscopy study of bubble growth in basaltic foam. *Nature Communications*. Nature Publishing Group UK London **3**, 1135.

Bamber, E. C., Arzilli, F., Polacci, M., Hartley, M. E., Fellowes, J., Di Genova, D., Chavarría, D., Saballos, J. A. & Burton, M. R. (2020). Pre- and syn-eruptive conditions of a basaltic Plinian eruption at Masaya Volcano, Nicaragua: The Masaya Triple Layer (2.1 ka). *Journal of Volcanology and Geothermal Research* **392**, 106761.

Bamber, E. C., La Spina, G., Arzilli, F., de'Michieli Vitturi, M., Polacci, M., Hartley, M. E., Petrelli, M., Fellowes, J. & Burton, M. (2022). Basaltic Plinian eruptions at Las Sierras-Masaya volcano driven by cool storage of crystal-rich magmas. *Communications Earth & Environment*. Nature Publishing Group UK London **3**, 253.

Behncke, B. & Neri, M. (2003). Cycles and trends in the recent eruptive behaviour of Mount Etna (Italy). *Canadian Journal of Earth Sciences*. NRC Research Press Ottawa, Canada **40**, 1405–1411.

Berger, A., Herwegh, M., Schwarz, J.-O. & Putlitz, B. (2011). Quantitative analysis of crystal/grain sizes and their distributions in 2D and 3D. *Journal of Structural Geology* **33**, 1751–1763.

Blundy, J. & Cashman, K. (2001). Ascent-driven crystallisation of dacite magmas at Mount St Helens, 1980–1986. *Contributions to Mineralogy and Petrology*. Springer **140**, 631–650.

Boschetty, F. O., Ferguson, D. J., Cortés, J. A., Morgado, E., Ebmeier, S. K., Morgan, D. J., Romero, J. E. & Parejas, C. S. (2022). Insights into magma storage beneath a frequently erupting arc volcano (Villarrica, Chile) from unsupervised machine learning analysis of mineral compositions. *Geochemistry, Geophysics, Geosystems*. Wiley Online Library **23**, e2022GC010333.

Brady, J. & Perkins, D. (2017). Mineral formulae recalculation. *SERC Carleton College http://serc. carleton. edu/research_education/equilibria/mineralformulaerecalculation. html. Accessed* **31**.

Branca, S., Coltelli, M. & Groppelli, G. (2004). Geological evolution of Etna volcano. *Washington DC American Geophysical Union Geophysical Monograph Series* **143**, 49–63.

Branca, S. & Del Carlo, P. (2005). Types of eruptions of Etna volcano AD 1670–2003: implications for short-term eruptive behaviour. *Bulletin of Volcanology*. Springer **67**, 732–742.

Brandeis, G. & Jaupart, C. (1986). On the interaction between convection and crystallization in cooling magma chambers. *Earth and Planetary Science Letters* **77**, 345–361.

Breiman, L. (2002). Manual on setting up, using, and understanding random forests v3. 1. *Statistics Department University of California Berkeley, CA, USA* **1**, 3–42.

Brugger, C. R. & Hammer, J. E. (2010). Crystal size distribution analysis of plagioclase in experimentally decompressed hydrous rhyodacite magma. *Earth and Planetary Science Letters* **300**, 246–254.

Cagney, N. & Balabani, S. (2019). Taylor-Couette flow of shear-thinning fluids. *Physics of Fluids*. AIP Publishing **31**.

Calvari, S. & Nunnari, G. (2022). Comparison between Automated and Manual Detection of Lava Fountains from Fixed Monitoring Thermal Cameras at Etna Volcano, Italy. *Remote Sensing*. MDPI **14**, 2392.

Cappello, A., Bilotta, G., Neri, M. & Negro, C. D. (2013). Probabilistic modeling of future volcanic eruptions at Mount Etna. *Journal of Geophysical Research: Solid Earth*. Wiley Online Library **118**, 1925–1935.

Caricchi, L. & Blundy, J. (2015). Experimental petrology of monotonous intermediate magmas. *Geological Society, London, Special Publications*. Geological Society of London **422**, 105–130.

Caricchi, L., Burlini, L., Ulmer, P., Gerya, T., Vassalli, M. & Papale, P. (2007). Non-Newtonian rheology of crystal-bearing magmas and implications for magma ascent dynamics. *Earth and Planetary Science Letters* **264**, 402–419.

Caricchi, L., Petrelli, M., Bali, E., Sheldrake, T., Pioli, L. & Simpson, G. (2020). A data driven approach to investigate the chemical variability of clinopyroxenes from the 2014–2015 Holuhraun–Bárdarbunga Eruption (Iceland). *Frontiers in Earth Science*. Frontiers **8**, 18.

Cashman, K. & Blundy, J. (2000). Degassing and crystallization of ascending andesite and dacite. *Philosophical Transactions of the Royal Society of London. Series A: Mathematical, Physical and Engineering Sciences*. The Royal Society **358**, 1487–1513.

Cashman, K. V. (2020). Crystal Size Distribution (CSD) Analysis of Volcanic Samples: Advances and Challenges. *Frontiers in Earth Science* **8**.

Cashman, K. V. & Ferry, J. M. (1988). Crystal size distribution (CSD) in rocks and the kinetics and dynamics of crystallization: III. Metamorphic crystallization. *Contributions to Mineralogy and Petrology*. Springer **99**, 401–415.

Cashman, K. V. & Marsh, B. D. (1988). Crystal size distribution (CSD) in rocks and the kinetics and dynamics of crystallization II: Makaopuhi lava lake. *Contributions to Mineralogy and Petrology*. Springer **99**, 292–305.

Cashman, K. V., Soule, S. A., Mackey, B. H., Deligne, N. I., Deardorff, N. D. & Dietterich, H. R. (2013). How lava flows: New insights from applications of lidar technologies to lava flow studies. *Geosphere*. GeoScienceWorld **9**, 1664–1680.

Cashman, K. V., Sparks, R. S. J. & Blundy, J. D. (2017). Vertically extensive and unstable magmatic systems: a unified view of igneous processes. *Science*. American Association for the Advancement of Science **355**, eaag3055.

Cassidy, M., Manga, M., Cashman, K. & Bachmann, O. (2018). Controls on explosive-effusive volcanic eruption styles. *Nature Communications*. Nature Publishing Group **9**, 2839.

Cassidy, M. & Mani, L. (2022). Huge volcanic eruptions: time to prepare. *Nature* **608**, 469–471.

Cheng, J., Gröbner, J., Hort, N., Kainer, K. U. & Schmid-Fetzer, R. (2014). Measurement and calculation of the viscosity of metals—a review of the current status and developing trends. *Measurement Science and Technology*. IOP Publishing **25**, 062001.

Chernov, A. A. (1974). Stability of faceted shapes. *Journal of Crystal Growth*. Elsevier **24**, 11–31.

Chevrel, M. O., Cimarelli, C., deBiasi, L., Hanson, J. B., Lavallée, Y., Arzilli, F. & Dingwell, D. B. (2015). Viscosity measurements of crystallizing andesite from Tungurahua volcano (Ecuador). *Geochemistry, Geophysics, Geosystems* **16**, 870–889.

Corsaro, R. A. & Miraglia, L. (2022). Near Real-Time Petrologic Monitoring on Volcanic Glass to Infer Magmatic Processes During the February–April 2021 Paroxysms of the South-East Crater, Etna. *Frontiers in Earth Science* **10**.

Couch, S., Harford, C. L., Sparks, R. S. J. & Carroll, M. R. (2003). Experimental constraints on the conditions of formation of highly calcic plagioclase microlites at the Soufrire Hills Volcano, Montserrat. *Journal of Petrology*. Oxford University Press **44**, 1455–1475.

De Campos, C. P., Perugini, D., Petrelli, M., Kolzenburg, S., Dorfman, A. & Dingwell, D. B. (2011). Mixing Experiments with Natural Shoshonitic and Trachytic Melts: A comparative Study Under Contrasting Rheological and Fluid Dynamic Conditions. *GEOPHYSICAL RESEARCH ABSTRACTS*, 11533–11533.

Demurtas, M., Smith, S. A. F., Prior, D. J., Spagnuolo, E. & Di Toro, G. (2019). Development of crystallographic preferred orientation during cataclasis in low-temperature carbonate fault gouge. *Journal of Structural Geology* **126**, 37–50.

Di Fiore, F. *et al.* (2023). Experimental Constraints on the Rheology of Lavas From 2021 Cumbre Vieja Eruption (La Palma, Spain). *Geophysical Research Letters* **50**, e2022GL100970.

Di Fiore, F., Vona, A., Costa, A., Mollo, S. & Romano, C. (2022). Quantifying the influence of cooling and shear rate on the disequilibrium rheology of a trachybasaltic melt from Mt. Etna. *Earth and Planetary Science Letters* **594**, 117725.

Di Fiore, F., Vona, A., Di Genova, D., Pontesilli, A., Calabrò, L., Mollo, S., Taddeucci, J., Romano, C. & Scarlato, P. (2024). Magma titanium and iron contents dictate crystallization timescales and rheological behaviour in basaltic volcanic systems. *Communications Earth & Environment*. Nature Publishing Group **5**, 283.

Di Fiore, F., Vona, A., Kolzenburg, S., Mollo, S. & Romano, C. (2021). An Extended Rheological Map of Pāhoehoe—‘A‘ā Transition. *Journal of Geophysical Research: Solid Earth* **126**, e2021JB022035.

Di Palma, M. A. & Gallo, M. (2016). A co-median approach to detect compositional outliers. *Journal of Applied Statistics*. Taylor & Francis **43**, 2348–2362.

Dingwell, D. B. & Virgo, D. (1987). The effect of oxidation state on the viscosity of melts in the system Na2O-FeO-Fe2O3-SiO2. *Geochimica et Cosmochimica Acta*. Elsevier **51**, 195–205.

Dingwell, D. B. & Virgo, D. (1988). Viscosities of melts in the Na2O□ FeO□ Fe2O3□ SiO2 system and factors controlling relative viscosities of fully polymerized silicate melts. *Geochimica et Cosmochimica Acta*. Elsevier **52**, 395–403.

Donnelly, R. J. (1991). Taylor-Couette flow: The early days. *Physics Today*. American Institute of Physics **44**, 32–39.

Eesa, A. S. & Arabo, W. K. (2017). A normalization methods for backpropagation: a comparative study. *Science Journal of University of Zakho* **5**, 319–323.

Egozcue, J. J., Pawlowsky-Glahn, V., Mateu-Figueras, G. & Barcelo-Vidal, C. (2003). Isometric logratio transformations for compositional data analysis. *Mathematical geology*. Springer **35**, 279–300.

Feldmann, D., Borrero-Echeverry, D., Burin, M. J., Avila, K. & Avila, M. (2023). Routes to turbulence in Taylor–Couette flow. *Philosophical Transactions of the Royal Society A: Mathematical, Physical and Engineering Sciences*. Royal Society **381**, 20220114.

Ferracutti, G. R., Asiain, L. M., Antonini, A. S., Tanzola, J. E. & Ganuza, M. L. (2024). OxyEMG: an application for determination of the oxyspinel group end-members based on electron microprobe analyses. European Journal of Mineralogy. Copernicus GmbH 36, 87–98.

First, E. C., Leonhardi, T. C., & Hammer, J. E. (2020). Effects of superheating magnitude on olivine growth. Contributions to Mineralogy and Petrology, 175(2), 13.

Freda, C., Gaeta, M., Giaccio, B., Marra, F., Palladino, D. M., Scarlato, P. & Sottili, G. (2011). CO2-driven large mafic explosive eruptions: the Pozzolane Rosse case study from the Colli Albani Volcanic District (Italy). Bulletin of Volcanology 73, 241–256.

Freire, S., Florczyk, A. J., Pesaresi, M. & Sliuzas, R. (2019). An Improved Global Analysis of Population Distribution in Proximity to Active Volcanoes, 1975–2015. *ISPRS International Journal of Geo-Information*. Multidisciplinary Digital Publishing Institute **8**, 341.

Frontoni, A., Costa, A., Vona, A. & Romano, C. (2022). A comprehensive database of crystal-bearing magmas for the calibration of a rheological model. *Scientific Data*. Nature Publishing Group **9**, 247.

Giordano, D., Russell, J. K. & Dingwell, D. B. (2008). Viscosity of magmatic liquids: a model. *Earth and Planetary Science Letters*. Elsevier **271**, 123–134.

Gualda, G. A. R., Ghiorso, M. S., Lemons, R. V. & Carley, T. L. (2012). Rhyolite-MELTS: a Modified Calibration of MELTS Optimized for Silica-rich, Fluid-bearing Magmatic Systems. *Journal of Petrology* **53**, 875–890.

Hammer, J. E. & Rutherford, M. J. (2002). An experimental study of the kinetics of decompression-induced crystallization in silicic melt. *Journal of Geophysical Research: Solid Earth* **107**, ECV 8-1-ECV 8-24.

Higgins, M. D. (1999). Origin of megacrysts in granitoids by textural coarsening: a crystal size distribution (CSD) study of microcline in the Cathedral Peak Granodiorite, Sierra Nevada, California. *Geological Society, London, Special Publications*. The Geological Society of London **168**, 207–219.

Higgins, M. D. (2000). Measurement of crystal size distributions. *American Mineralogist*. Mineralogical Society of America **85**, 1105–1116.

Higgins, M. D. (2002). A crystal size-distribution study of the Kiglapait layered mafic intrusion, Labrador, Canada: evidence for textural coarsening. *Contributions to mineralogy and petrology*. Springer **144**, 314–330.

Higgins, M. D. (2011). Textural coarsening in igneous rocks. *International Geology Review*. Taylor & Francis **53**, 354–376.

Higgins, O., Sheldrake, T. & Caricchi, L. (2022). Machine learning thermobarometry and chemometry using amphibole and clinopyroxene: a window into the roots of an arc volcano (Mount Liamuiga, Saint Kitts). *Contributions to Mineralogy and Petrology*. Springer **177**, 1–22.

Ishibashi, H. & Sato, H. (2007). Viscosity measurements of subliquidus magmas: Alkali olivine basalt from the Higashi-Matsuura district, Southwest Japan. *Journal of Volcanology and Geothermal Research* **160**, 223–238.

Jorgenson, C., Higgins, O., Petrelli, M., Bégué, F. & Caricchi, L. (2022). A Machine Learning-Based Approach to Clinopyroxene Thermobarometry: Model Optimization and Distribution for Use in Earth Sciences. *Journal of Geophysical Research: Solid Earth*. Wiley Online Library **127**, e2021JB022904.

Kandlbauer, J., Hopcroft, P. O., Valdes, P. J. & Sparks, R. S. J. (2013). Climate and carbon cycle response to the 1815 Tambora volcanic eruption. *Journal of Geophysical Research: Atmospheres* **118**, 12,497-12,507.

Kirkpatrick, R. J. (1975). Crystal growth from the melt: a review. *American Mineralogist: Journal of Earth and Planetary Materials*. Mineralogical Society of America **60**, 798–814.

Kolzenburg, S., Chevrel, M. O. & Dingwell, D. B. (2022). Magma/suspension rheology. *Reviews in Mineralogy and Geochemistry*. Mineralogical Society of America **87**, 639–720.

Kolzenburg, S., Giordano, D., Hess, K. U. & Dingwell, D. B. (2018a). Shear rate-dependent disequilibrium rheology and dynamics of basalt solidification. *Geophysical Research Letters*. Wiley Online Library **45**, 6466–6475.

Kolzenburg, S., Giordano, D., Thordarson, T., Höskuldsson, A. & Dingwell, D. B. (2017). The rheological evolution of the 2014/2015 eruption at Holuhraun, central Iceland. *Bulletin of Volcanology* **79**, 45.

Kolzenburg, S., Jaenicke, J., Münzer, U. & Dingwell, D. B. (2018b). The effect of inflation on the morphology-derived rheological parameters of lava flows and its implications for interpreting remote sensing data-A case study on the 2014/2015 eruption at Holuhraun, Iceland. *Journal of Volcanology and Geothermal Research*. Elsevier **357**, 200–212.

Kouchi, A., Sugawara, Y., Kashima, K. & Sunagawa, I. (1983). Laboratory growth of sector zoned clinopyroxenes in the system CaMgSi 2 O 6-CaTiAl 2 O 6. *Contributions to Mineralogy and Petrology*. Springer **83**, 177–184.

Kouchi, A., Tsuchiyama, A. & Sunagawa, I. (1986). Effect of stirring on crystallization kinetics of basalt: texture and element partitioning. *Contributions to Mineralogy and Petrology* **93**, 429–438.

La Spina, G. *et al.* (2021). Explosivity of basaltic lava fountains is controlled by magma rheology, ascent rate and outgassing. *Earth and Planetary Science Letters* **553**, 116658.

La Spina, G., Burton, M. & Vitturi, M. de'Michieli (2015). Temperature evolution during magma ascent in basaltic effusive eruptions: A numerical application to Stromboli volcano. *Earth and Planetary Science Letters*. Elsevier **426**, 89–100.

Lanari, P., Vidal, O., De Andrade, V., Dubacq, B., Lewin, E., Grosch, E. G. & Schwartz, S. (2014). XMapTools: A MATLAB©-based program for electron microprobe X-ray image processing and geothermobarometry. *Computers & Geosciences*. Elsevier **62**, 227–240.

Lejeune, A.-M. & Richet, P. (1995). Rheology of crystal-bearing silicate melts: An experimental study at high viscosities. *Journal of Geophysical Research: Solid Earth* **100**, 4215–4229.

Lofgren, G. (2014). Chapter 11. Experimental Studies on the Dynamic Crystallization of Silicate Melts. *Physics of Magmatic Processes*. Princeton University Press, 487–552.

Mahalanobis, P. C. (1936). On the generalized distance in statistics. National Institute of Science of India.

Mainprice, D., Bachmann, F., Hielscher, R. & Schaeben, H. (2015). Descriptive tools for the analysis of texture projects with large datasets using MTEX: strength, symmetry and components. *Geological Society, London, Special Publications*. The Geological Society of London London **409**, 251–271.

Malawani, M. N., Lavigne, F., Gomez, C., Mutaqin, B. W. & Hadmoko, D. S. (2021). Review of Local and Global Impacts of Volcanic Eruptions and Disaster Management Practices: The Indonesian Example. *Geosciences*. Multidisciplinary Digital Publishing Institute **11**, 109.

Mangler, M. F., Humphreys, M. C. S., Wadsworth, F. B., Iveson, A. A. & Higgins, M. D. (2022). Variation of plagioclase shape with size in intermediate magmas: a window into incipient plagioclase crystallisation. *Contributions to Mineralogy and Petrology* **177**, 64.

Mani, L., Tzachor, A. & Cole, P. (2021). Global catastrophic risk from lower magnitude volcanic eruptions. *Nature Communications*. Nature Publishing Group **12**, 4756.

Meth, C. E. & Carlson, W. D. (2005). DIFFUSION-CONTROLLED SYNKINEMATIC GROWTH OF GARNET FROM A HETEROGENEOUS PRECURSOR AT PASSO DEL SOLE, SWITZERLAND. *The Canadian Mineralogist* **43**, 157–182.

Mills, R. D. & Glazner, A. F. (2013). Experimental study on the effects of temperature cycling on coarsening of plagioclase and olivine in an alkali basalt. *Contributions to Mineralogy and Petrology* **166**, 97–111.

Mills, R. D., Ratner, J. J. & Glazner, A. F. (2011). Experimental evidence for crystal coarsening and fabric development during temperature cycling. *Geology* **39**, 1139–1142.

Mock, A. & Jerram, D. A. (2005). Crystal size distributions (CSD) in three dimensions: insights from the 3D reconstruction of a highly porphyritic rhyolite. *Journal of Petrology*. Oxford University Press **46**, 1525–1541.

Moitra, P., Gonnermann, H. M., Houghton, B. F. & Tiwary, C. S. (2018). Fragmentation and Plinian eruption of crystallizing basaltic magma. *Earth and Planetary Science Letters* **500**, 97–104.

Mollo, S., Blundy, J. D., Iezzi, G., Scarlato, P. & Langone, A. (2013). The partitioning of trace elements between clinopyroxene and trachybasaltic melt during rapid cooling and crystal growth. *Contributions to Mineralogy and Petrology* **166**, 1633–1654.

Mollo, S., Del Gaudio, P., Ventura, G., Iezzi, G. & Scarlato, P. (2010). Dependence of clinopyroxene composition on cooling rate in basaltic magmas: Implications for thermobarometry. *Lithos* **118**, 302–312.

Mollo, S. & Hammer, J. E. (2017). Dynamic crystallization in magmas. *EMU Notes Mineral* **16**, 373–418.

Mollo, S., Pontesilli, A., Moschini, P., Palummo, F., Taddeucci, J., Andronico, D., Bello, E. D. & Scarlato, P. (2022). Modeling the crystallization conditions of clinopyroxene crystals erupted during February–April 2021 lava fountains at Mt. Etna: Implications for the dynamic transfer of magmas. *Lithos* **420–421**, 106710.

Mollo, S., Di Fiore, F., MacDonald, A., Ubide, T., Pontesilli, A., Giuliani, G., ... & Scarlato, P. (2024). Thermodynamics and kinetics of cation partitioning between plagioclase and trachybasaltic melt in static and dynamic systems: A reassessment of the lattice strain and electrostatic energies of substitution. Geochimica et Cosmochimica Acta, 384, 27-43.

Mondy, L. A., Brenner, H., Altobelli, S. A., Abbott, J. R. & Graham, A. L. (1994). Shear-induced particle migration in suspensions of rods. Journal of Rheology. The Society of Rheology 38, 444–452.

Morgavi, D., Perugini, D., De Campos, C. P., Ertl-Ingrisch, W., Lavallée, Y., Morgan, L. & Dingwell, D. B. (2013). Interactions between rhyolitic and basaltic melts unraveled by chaotic mixing experiments. Chemical Geology 346, 199–212.

Morgavi, D., Petrelli, M., Vetere, F. P., González-García, D. & Perugini, D. (2015). High-temperature apparatus for chaotic mixing of natural silicate melts. Review of Scientific Instruments. AIP Publishing 86.

Musu, A., Corsaro, R. A., Higgins, O., Jorgenson, C., Petrelli, M. & Caricchi, L. (2023). The magmatic evolution of South-East Crater (Mt. Etna) during the February–April 2021 sequence of lava fountains from a mineral chemistry perspective. Bulletin of Volcanology. Springer 85, 33.

Musu, A., Parodi, V., Toplak, M., Carfì, A., López, M. Á., Mastrogiovanni, F., ... & Petrelli, M. (2025). Orange and Orange-Volcanoes: a New Open and Collaborative Platform to Perform Data-Driven Investigations and Machine Learning Analyses in Petrology and Volcanology.

Nabelek, P. I., Whittington, A. G. & Sirbescu, M.-L. C. (2010). The role of H2O in rapid emplacement and crystallization of granite pegmatites: resolving the paradox of large crystals in highly undercooled melts. Contributions to Mineralogy and Petrology 160, 313–325.

Nicolas, A. & Ildefonse, B. (1996). Flow mechanism and viscosity in basaltic magma chambers. *Geophysical Research Letters* **23**, 2013–2016.

Okumura, S. H., Mujin, M., Tsuchiyama, A. & Miyake, A. (2022). 3D crystal size distributions of pyroxene nanolites from nano X-ray computed tomography: Improved correction of crystal size distributions from CSDCorrections for magma ascent dynamics in conduits. *American Mineralogist*. De Gruyter **107**, 1766–1778.

Papale, P. (1999). Strain-induced magma fragmentation in explosive eruptions. *Nature*. Nature Publishing Group **397**, 425–428.

Papale, P., Garg, D. & Marzocchi, W. (2022). Global Rates of Subaerial Volcanism on Earth. *Frontiers in Earth Science*. Frontiers **10**.

Perugini, D. (2021). *Mixing of Magmas*. Springer.

Perugini, D., De Campos, C. P., Dingwell, D. B., Petrelli, M. & Poli, G. (2008). Trace element mobility during magma mixing: preliminary experimental results. *Chemical Geology*. Elsevier **256**, 146–157.

Petrelli, M. (2023). *Machine Learning for Earth Sciences: Using Python to Solve Geological Problems*. Cham: Springer International Publishing.

Petrelli, M. (2024). Machine Learning in Petrology: State-of-the-Art and Future Perspectives. *Journal of Petrology* **65**, egae036.

Petrelli, M., Caricchi, L. & Perugini, D. (2020). Machine learning thermo-barometry: Application to clinopyroxene-bearing magmas. *Journal of Geophysical Research: Solid Earth*. Wiley Online Library **125**, e2020JB020130.

Petrelli, M., El Omari, K., Spina, L., Le Guer, Y., La Spina, G. & Perugini, D. (2018). Timescales of water accumulation in magmas and implications for short warning times of explosive eruptions. *Nature Communications*. Nature Publishing Group **9**, 770.

Piombo, A. & Dragoni, M. (2009). Evaluation of flow rate for a one-dimensional lava flow with power-law rheology. *Geophysical Research Letters* **36**.

Qin, Z. & Suckale, J. (2020). Flow-to-sliding transition in crystal-bearing magma. *Journal of Geophysical Research: Solid Earth*. Wiley Online Library **125**, e2019JB018549.

R Core Team (2021). R: A language and environment for statistical computing. R. R Foundation for Statistical Computing, Vienna, Austria. URL:https://www.R-project.org/.

Rousseeuw, P. J. & Hubert, M. (2011). Robust statistics for outlier detection. *Wiley interdisciplinary reviews: Data mining and knowledge discovery*. Wiley Online Library **1**, 73–79.

Rubin, A. M. (1995). Propagation of magma-filled cracks. *Annual Review Of Earth And Planetary Sciences, Volume 23, pp. 287-336.* **23**, 287–336.

Rusiecka, M. K., Bilodeau, M. & Baker, D. R. (2020). Quantification of nucleation delay in magmatic systems: experimental and theoretical approach. *Contributions to Mineralogy and Petrology* **175**, 47.

Sable, J. E., Houghton, B. F., Del Carlo, P. & Coltelli, M. (2006). Changing conditions of magma ascent and fragmentation during the Etna 122 BC basaltic Plinian eruption: Evidence from clast microtextures. *Journal of Volcanology and Geothermal Research* **158**, 333–354.

Sarabian, M., Firouznia, M., Metzger, B. & Hormozi, S. (2019). Fully developed and transient concentration profiles of particulate suspensions sheared in a cylindrical Couette cell. *Journal of Fluid Mechanics*. Cambridge University Press **862**, 659–671.

Shea, T. & Hammer, J. E. (2013). Kinetics of cooling- and decompression-induced crystallization in hydrous mafic-intermediate magmas. *Journal of Volcanology and Geothermal Research* **260**, 127–145.

Shinbrot, T., Alexander, A. & Muzzio, F. J. (1999). Spontaneous chaotic granular mixing. *Nature*. Nature Publishing Group **397**, 675–678.

Simakin, A. G. & Bindeman, I. N. (2008). Evolution of crystal sizes in the series of dissolution and precipitation events in open magma systems. *Journal of Volcanology and Geothermal Research*. Elsevier **177**, 997–1010.

Simkin, T., Siebert, L., McClelland, L., Bridge, D., Newhall, C. & Latter, J. H. (1994). *Volcanoes of the World*. Geoscience Press, TusconAZ.

Spina, L., Cannata, A., Morgavi, D. & Perugini, D. (2019). Degassing behaviour at basaltic volcanoes: New insights from experimental investigations of different conduit geometry and magma viscosity. *Earth-science reviews*. Elsevier **192**, 317–336.

Sunagawa, I. (1999). Growth and morphology of crystals. *FORMA-TOKYO-* **14**, 147–166.

Szramek, L. A. (2016). Mafic Plinian eruptions: Is fast ascent required? *Journal of Geophysical Research: Solid Earth* **121**, 7119–7136.

Taylor, G. I. (1923). VIII. Stability of a viscous liquid contained between two rotating cylinders. *Philosophical Transactions of the Royal Society of London. Series A, Containing Papers of a Mathematical or Physical Character*. The Royal Society London **223**, 289–343.

Templ, M., Filzmoser, P. & Reimann, C. (2008). Cluster analysis applied to regional geochemical data: Problems and possibilities. *Applied Geochemistry* **23**, 2198–2213.

Toorman, E. A. (1994). An analytical solution for the velocity and shear rate distribution of non-ideal Bingham fluids in concentric cylinder viscometers. *Rheologica Acta*. Springer **33**, 193–202.

Toramaru, A. (2022). CSD (Crystal Size Distribution). *Vesiculation and Crystallization of Magma*. Singapore: Springer Singapore, 301–347.

Toschev, S. (1973). Homogeneous nucleation. *(Hartman P) Crystal growth—an introduction*. New York: Elsevier, PP. 1-49.

Tripoli, B., Manga, M., Mayeux, J. & Barnard, H. (2019). The Effects of Deformation on the Early Crystallization Kinetics of Basaltic Magmas. *Frontiers in Earth Science*. Frontiers **7**.

Ubide, T., Mollo, S., Zhao, J., Nazzari, M. & Scarlato, P. (2019). Sector-zoned clinopyroxene as a recorder of magma history, eruption triggers, and ascent rates. *Geochimica et Cosmochimica Acta* **251**, 265–283.

Vetere, F. *et al.* (2024). The role of deformation on the early crystallization and rheology of basaltic liquids. *Earth and Planetary Science Letters* **644**, 118934.

Vetere, F., Iezzi, G., Perugini, D. & Holtz, F. (2022). Rheological changes in melts and magmas induced by crystallization and strain rate. *Comptes Rendus. Géoscience* **354**, 1–22.

Vetere, F., Murri, M., Alvaro, M., Domeneghetti, M. C., Rossi, S., Pisello, A., Perugini, D. & Holtz, F. (2019). Viscosity of pyroxenite melt and its evolution during cooling. *Journal of Geophysical Research: Planets*. Wiley Online Library **124**, 1451–1469.

Vetere, F., Petrelli, M., Perugini, D., Haselbach, S., Morgavi, D., Pisello, A., Iezzi, G. & Holtz, F. (2021). Rheological evolution of eruptible Basaltic-Andesite Magmas under dynamic conditions: The importance of plagioclase growth rates. *Journal of Volcanology and Geothermal Research* **420**, 107411.

Vetere, F., Rossi, S., Namur, O., Morgavi, D., Misiti, V., Mancinelli, P., Petrelli, M., Pauselli, C. & Perugini, D. (2017). Experimental constraints on the rheology, eruption, and emplacement dynamics of analog lavas comparable to Mercury's northern volcanic plains. *Journal of Geophysical Research: Planets* **122**, 1522–1538.

Vona, A. & Romano, C. (2013). The effects of undercooling and deformation rates on the crystallization kinetics of Stromboli and Etna basalts. *Contributions to Mineralogy and Petrology* **166**, 491–509.

Vona, A., Romano, C., Dingwell, D. B. & Giordano, D. (2011). The rheology of crystal-bearing basaltic magmas from Stromboli and Etna. *Geochimica et Cosmochimica Acta*. Pergamon **75**, 3214–3236.

Ward Jr, J. H. (1963). Hierarchical grouping to optimize an objective function. *Journal of the American statistical association*. Taylor & Francis **58**, 236–244.

Welsch, B., Hammer, J., Baronnet, A., Jacob, S., Hellebrand, E. & Sinton, J. (2016). Clinopyroxene in postshield Haleakala ankaramite: 2. Texture, compositional zoning and supersaturation in the magma. *Contributions to Mineralogy and Petrology* **171**, 6.

FIGURE CAPTIONS

Fig. 1 – a) sketch of the crucible with the spindle immersed in the melt. b) sketch of the rotating spindle with velocity (u) and shear strain rate (Ẏ) profiles within the melt-filled gap. c) schematic sketch of the experiment from the super-liquidus melting at 1400°C to the final quench after 84h.

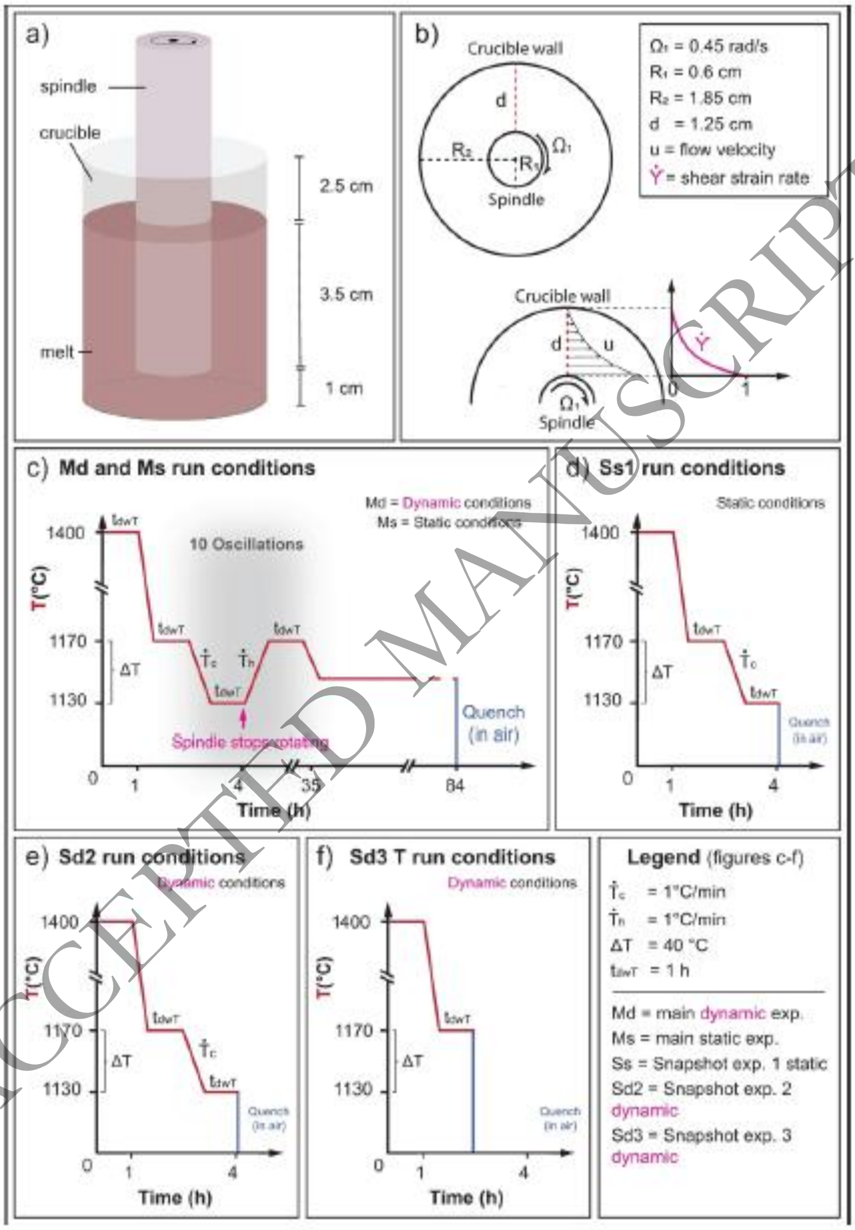

Fig 2 – BSE images comparison between the static (Ms; a) and the dynamic (Md; b) main experiments, far and close to the spindle. BSE images of the static (Ss1; c) and the dynamic (Sd2; d) snapshot experiments.

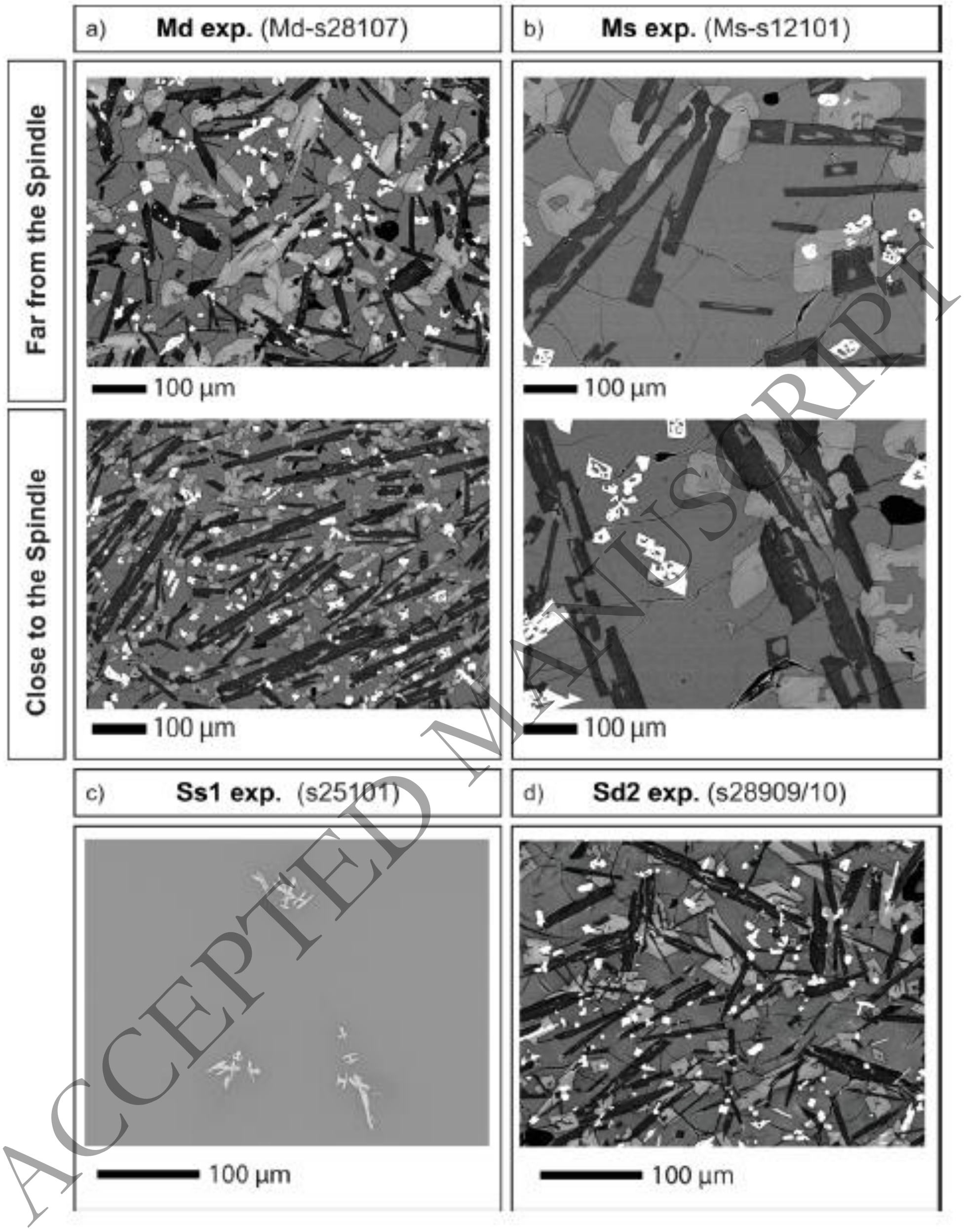

Fig. 3 – a)) Pl BSE images from sample Md-s28107. b) Cpx BSE images from the three different scans in sample Md-s28107. c) Zoom on Cpx oscillatory zoning. d) Fe-Spl BSE images from sample Md-s28107.

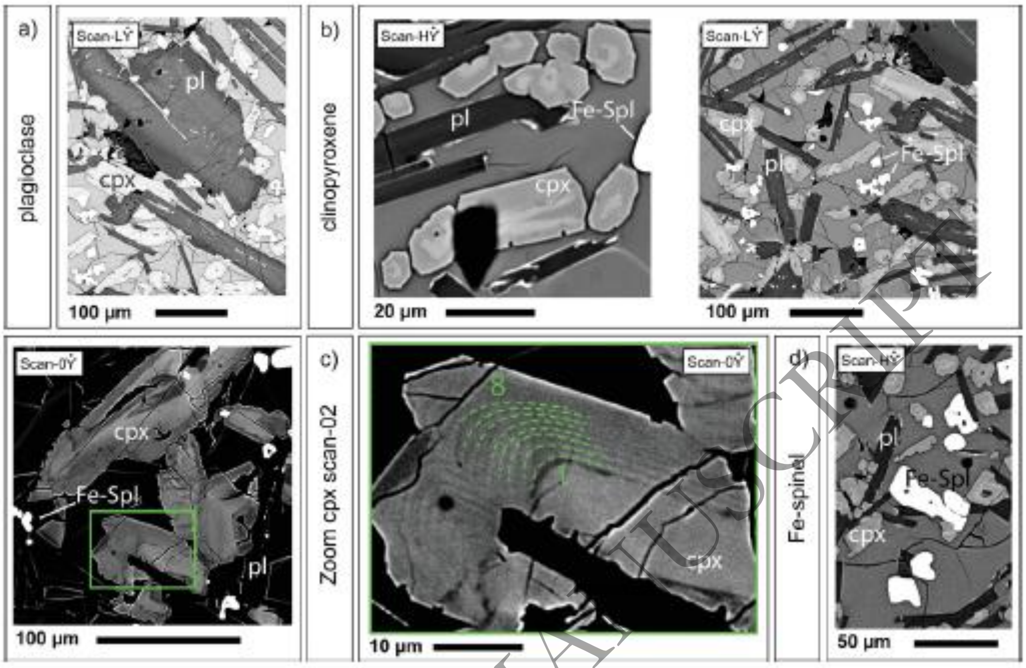

Fig. 4 – a, d, g) CSDs of all mineral phases in the three different scans (HẎ-0Ẏ). The CSD interpolation lines of the largest crystals, for each mineral phase, are reported with a continuous line coloured according to the phase colour. G_{MAX} and J_M values have been reported for each phase in each scan. b, e, h) Rose diagrams of the SPOs for each mineral phase in each scan, with quantitative Pl SPO strength. c, f, i) Stereographic, upper hemisphere, antipodal pole figure projections of orientation distribution functions (ODFs) describing the CPO of Pl and Cpx in each scan. All ODFs use mean grain orientations and a halfwidth of 15°. The plane pole / direction to which each pole figure corresponds is labelled directly above it. For each phase, the CPO strength (J_{ODF}) and number of grains (N) is given, along with the maximum (upper left of each pole figure) and minimum (lower left of each pole figure) intensity in each pole figure, in units of multiples of the uniform distribution. The colour map used is shown at the bottom of the figure. The pole figures and rose diagrams are oriented identically to the corresponding scans in Fig. 4. Thick black sub horizontal lines in rose diagrams and pole figures indicate the orientation of the plane parallel to the spindle surface. Dashed subvertical lines in pole figures indicate the trace of the radial direction. Shear sense is indicated to the left of rose diagrams.

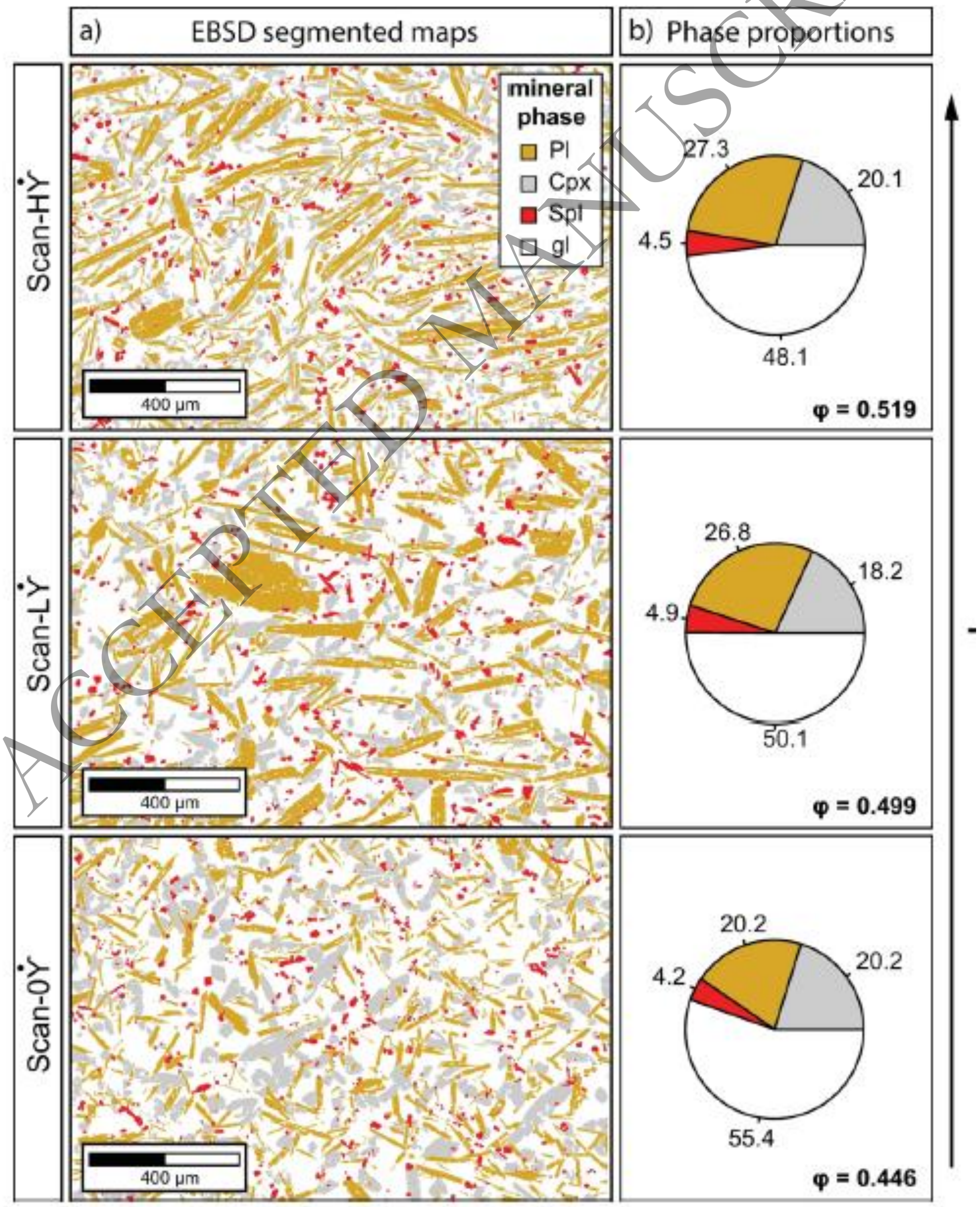

Fig. 5 – a) crops of the EBSD segmented scans (HẎ-0Ẏ), Pl are displayed in orange, Cpx in light grey and Fe-Spl in red. b) area phase proportions in each scan, the total crystallinity (φ) has been also reported for each scan.

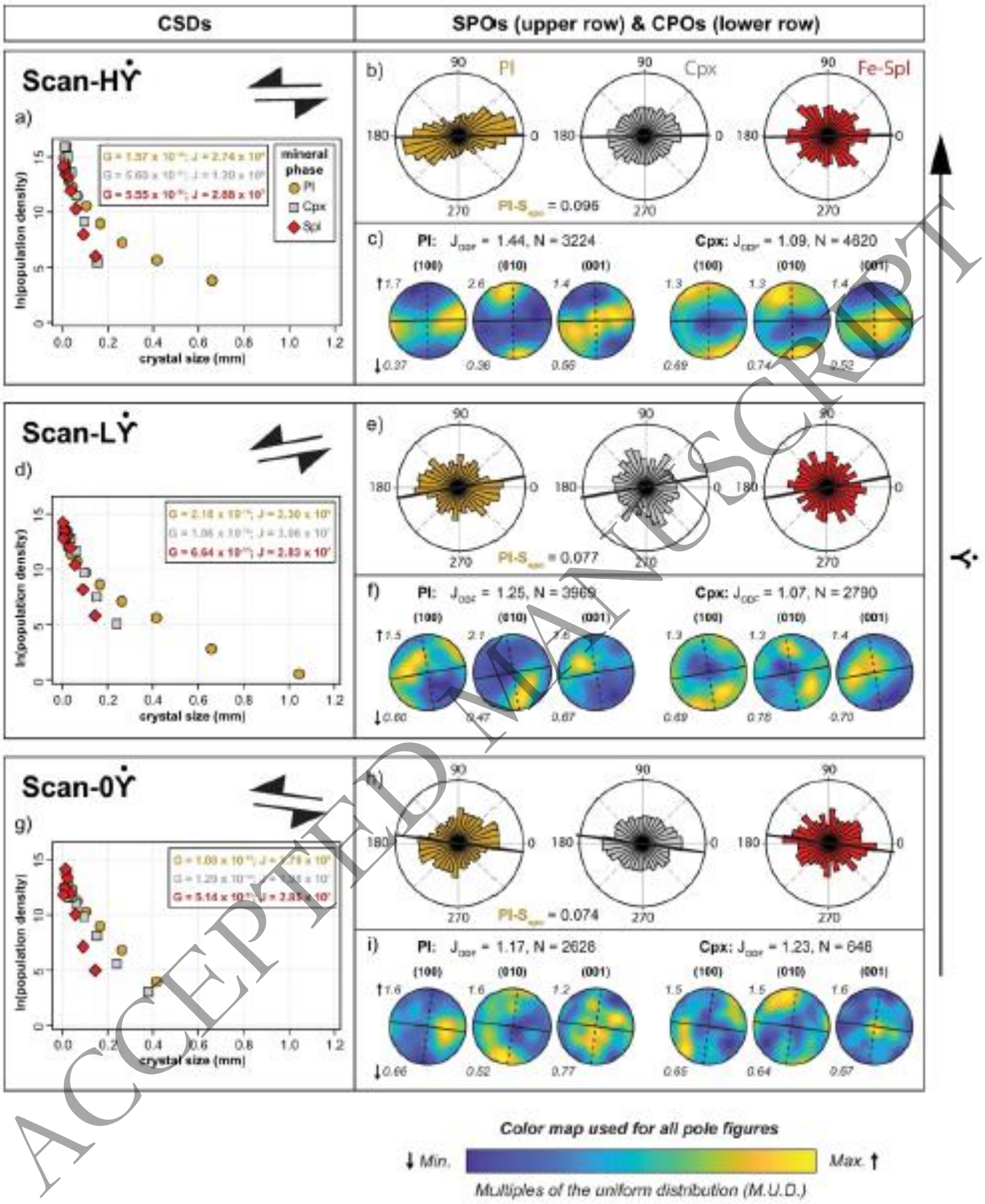

Fig. 6 – CSDs in the three scans of Pl (a,b), Cpx (c,d) and Fe-Spl (e,f). In figure a, c and e regression lines are reported for the CSD of all the crystal population (highlight by a red dot line the size cut-off between the two Pl population; a). In figure b, d and f we report CSD curves for all the mineral phases and the relative errors. Zooms on Pl CSD curves at small crystal sizes are highlighted in figure b.

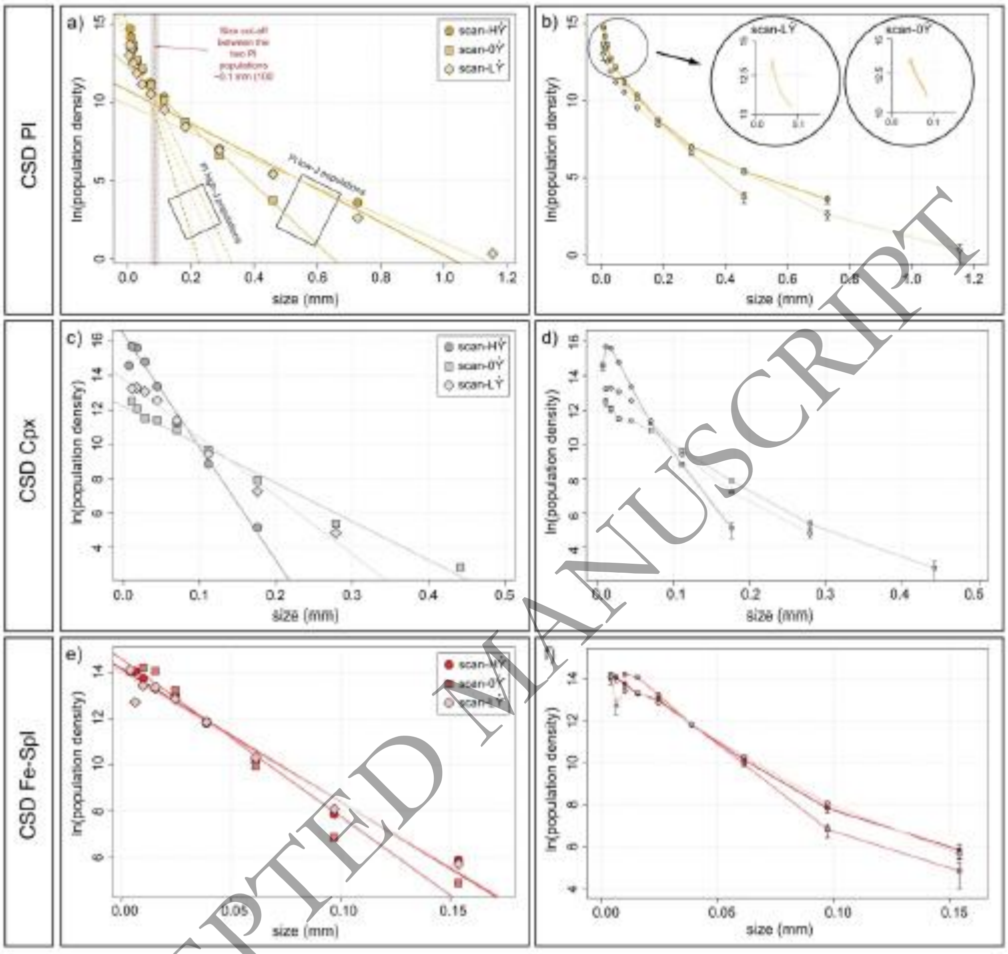

Fig. 7 – Oxide glass composition of sample Md-s28107 and Md-s28106 shown as MgO vs Al_2O_3 (a) and MgO vs SiO_2 (b). Analytical points acquired in scans-H′ϒ̇, -0′ϒ̇ and -L′ϒ̇ have been highlighted with larger pink, yellow and red dots respectively. The MgO, Al_2O_3 and SiO_2 average analytical uncertainties have been reported within all figures.

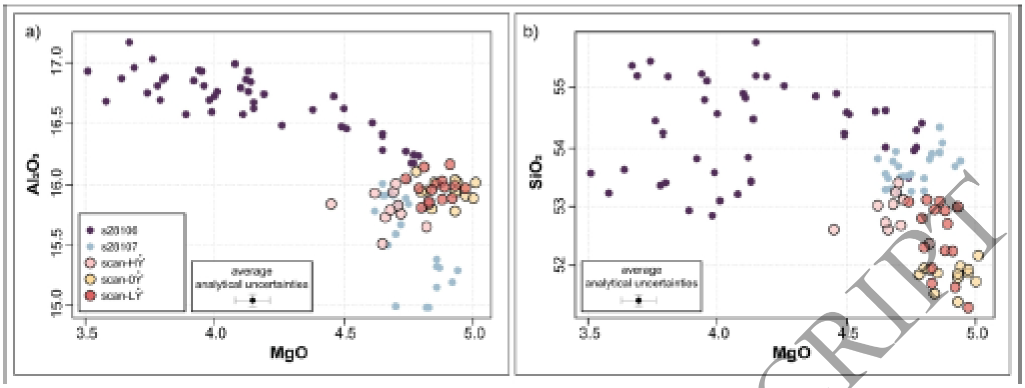

Fig. 8 – a) Violin plot reporting the main major oxides composition of clusters in each mineral phase (Pl, Cpx and Fe-spinel. b) FeO has been plotted against CaO for plagioclase, and the observation in the plot colour coded according to the cluster of belonging. Mg# and CaO/Al$_2$O$_3$ have been plotted against each other for Cpx and MgO against the Usp component for Fe-Spl. All the observations are colour coded according to the cluster of belongings.

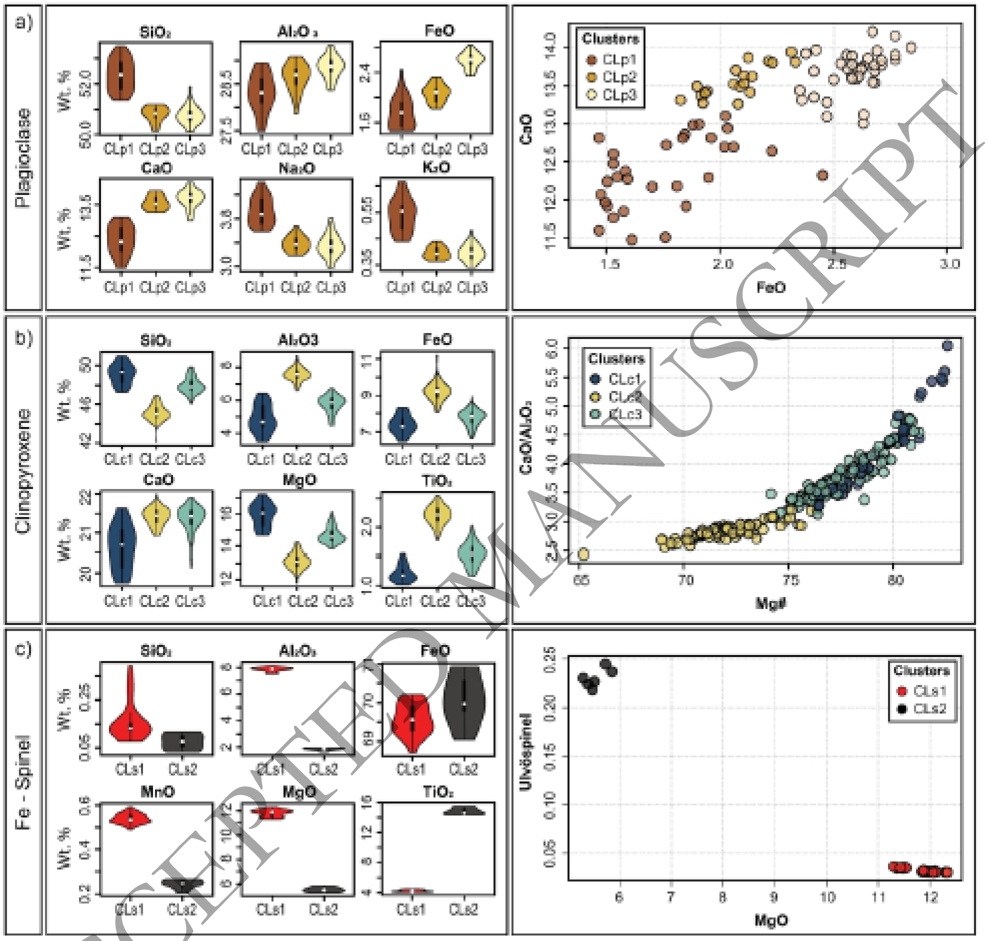

Fig. 9 – a) Clustered map for each mineral phase (Cpx, Pl, Fe-Spl) in each scan area. b) cluster area proportion in each mineral phase (for each scan) expressed as area percentage.

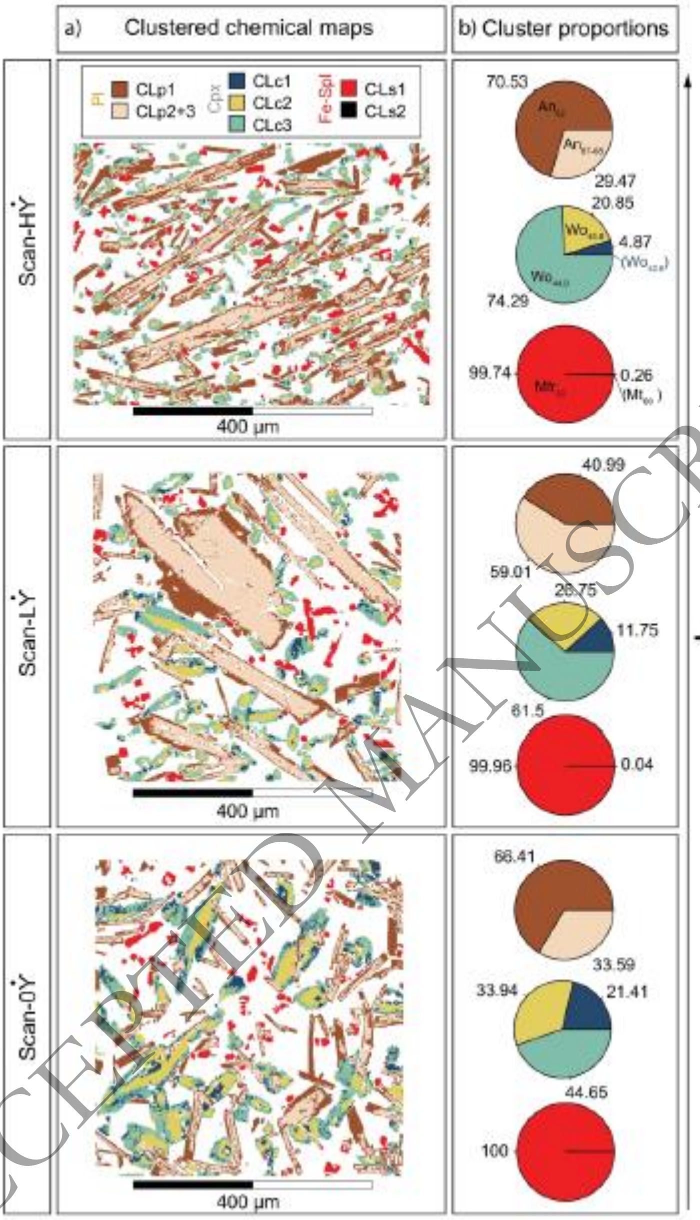

Fig. 10 – Sketch synthesizing the main crystal cluster formation events along the experiment.

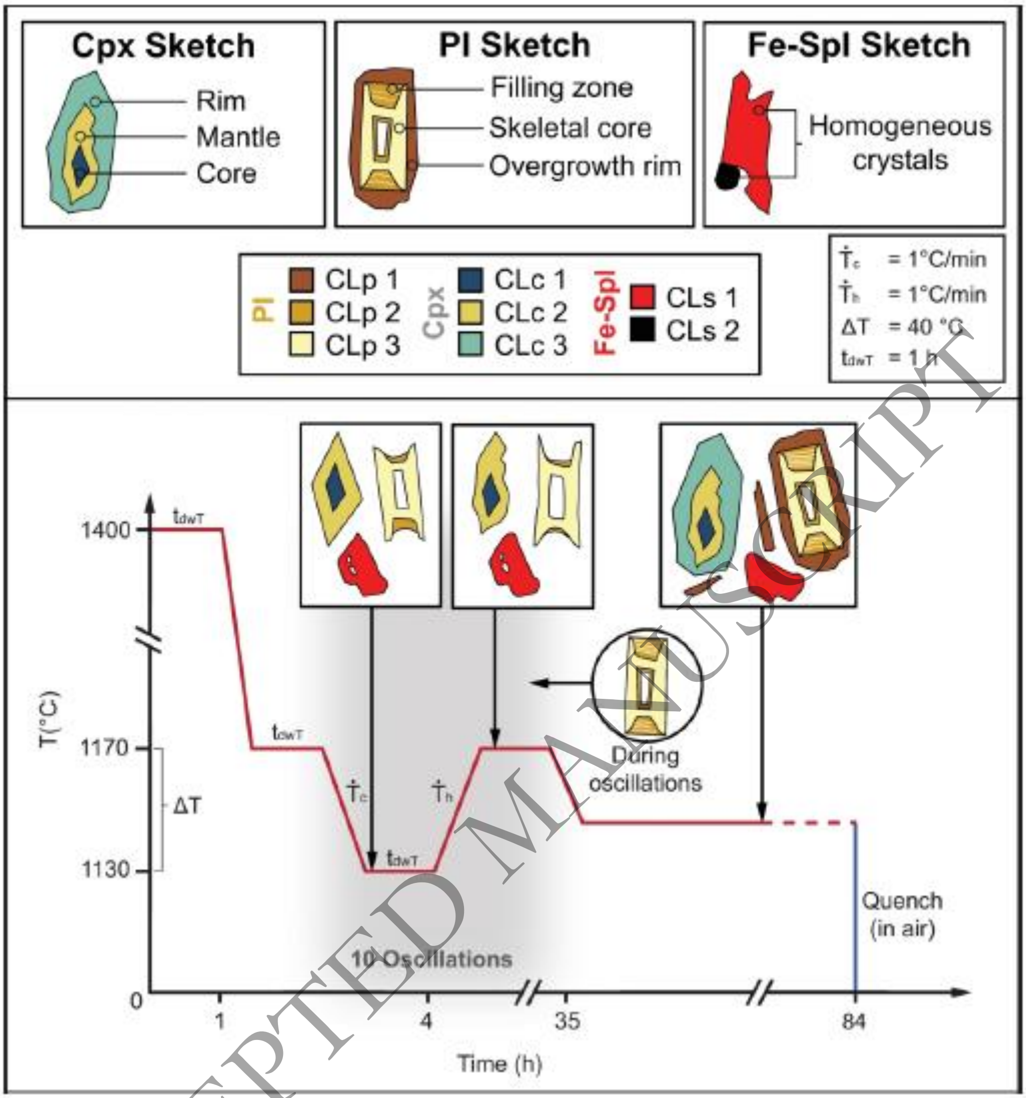

Fig. 11 – a) Pl, Cpx and Fe-Spl growth rates (G in m/s) plotted against the CPO strength. b) Pl, Cpx and Fe-Spl nucleation rates (J in 1/m^{3}s) plotted against the CPO strength. Error bars on G_{MAX} represent the standard error for G_{MAX} calculated from the ten largest crystals in each map, reflecting the precision of the mean estimate. Error bars on J_M represents uncertainties propagated error from crystal size correction and crystal count.

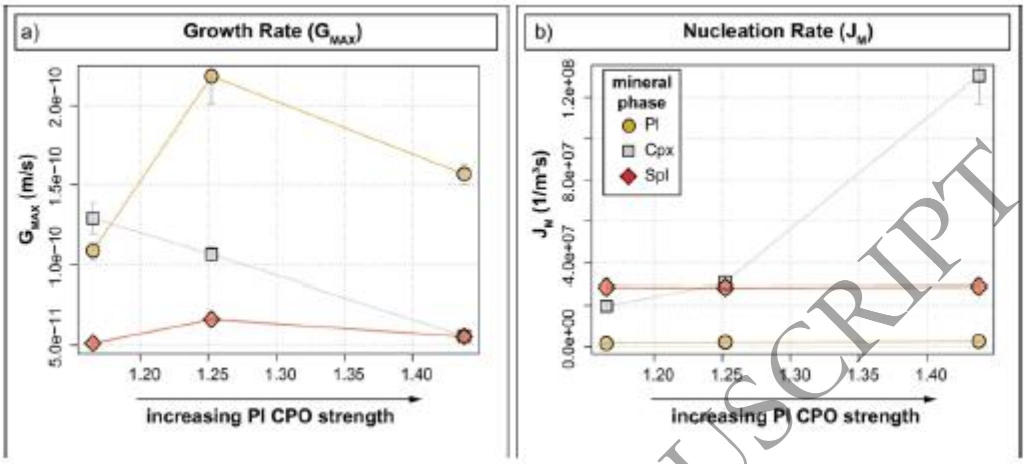

Fig. 12 – a) Pl CPO strength versus Pl fraction; b) Residual glass Mg# variation as a function of Pl/Cpx fraction variation.

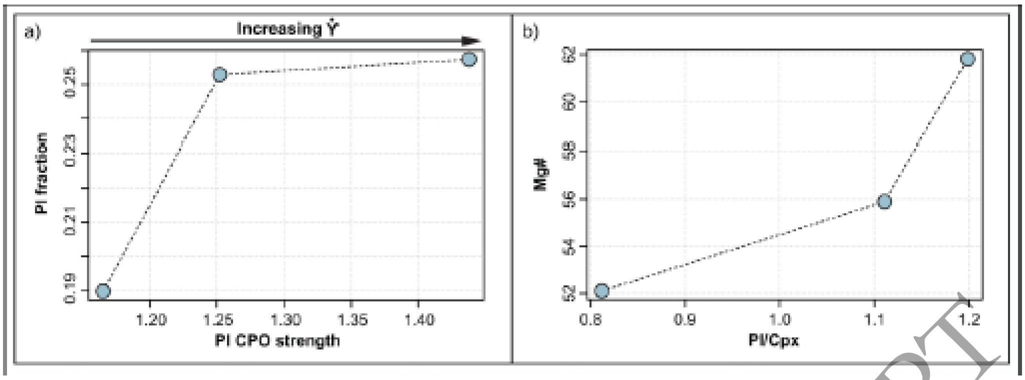

Fig. 13 – Comparison between natural glass variability (Musu et al., 2023), and experimental residual glass variability observed in this work (for MgO and Al_2O_3). The natural glass MgO and Al_2O_3 content is reported against the eruption event as red circles. The continuous black line fitting the Mt. Etna chemical variation in time pass through the median compositional values of each eruptive episode. On the right side of the plot, we report the compositional variability range measured in our experiments for MgO and Al_2O_3. As can be observed the chemical variation observed in our experiment is of the same order of magnitude that the one observed at Mt. Etna.

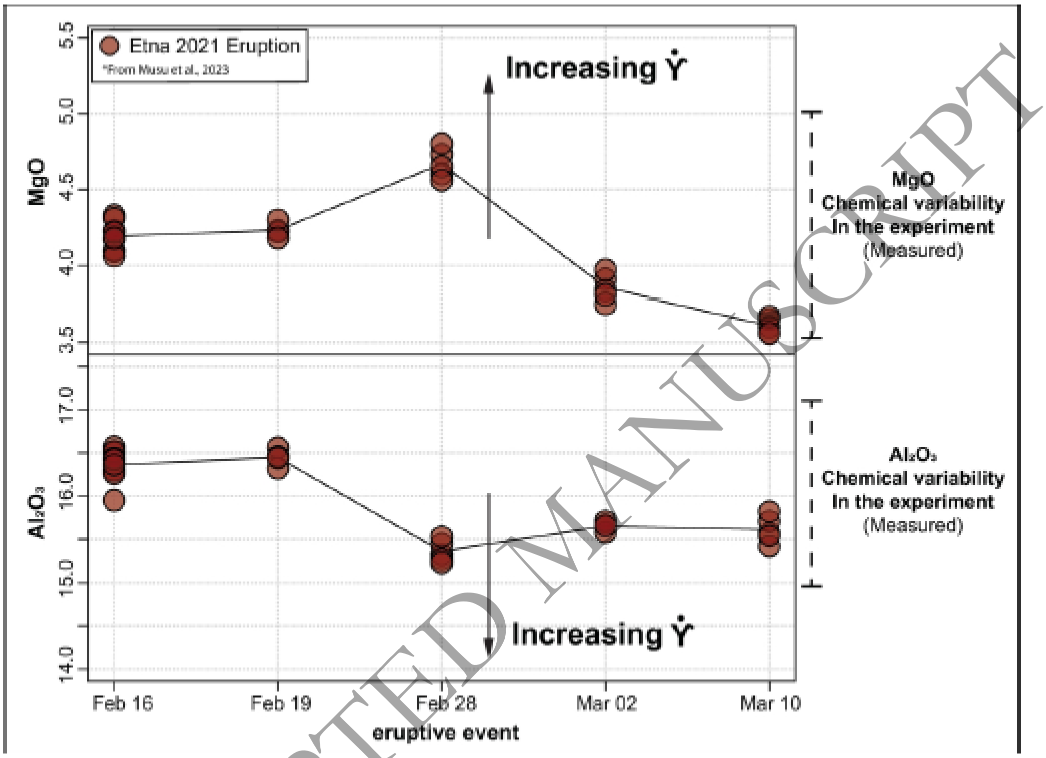

Table 1 – Starting glass composition.

	SiO_2	TiO_2	Al_2O_3	FeO	MgO	MnO	CaO	Na_2O	K_2O	Total
Mean wt%	47.44	1.72	16.10	10.03	5.99	0.19	10.62	3.37	1.91	97.38
Sd	0.20	0.03	0.08	0.11	0.06	0.03	0.05	0.08	0.03	0.34

Table 1 – Chemical composition of the starting glass used in this study (ETN02M). The reported oxide concentrations in wt % are the result of the average between the composition of 23 EPMA point acquire throughout the starting glass sample. We reported for each average oxide concentration the respective standard deviation (sd).

Table 2 – Apparent G and J as function of pl orientation

Scan	**phase**	**G_{MAX}** (m s^{-1})	**SE G_{MAX}**	**J_M** (m^{-3}s^{-1})	**σJ_M**	**pl CPO** strength	**N_A** (m^{-2})
Scan-HΎ̇	Pl	1.57E-10	0.20E-10	2.74E+06	6.45E-12	1.44	4.40E+07
Scan-LΎ̇	Pl	2.18E-10	0.55E-10	2.30E+06	1.73E-11	1.25	4.13E+07
Scan-0Ύ̇	Pl	1.08E-10	0.17E-10	1.70E+06	5.50E-12	1.17	2.16E+07
Scan-HΎ̇	Cpx	5.60E-11	0.29E-11	1.30E+08	1.04E-12	1.44	5.48E+08
Scan-LΎ̇	Cpx	1.06E-10	0.14E-10	3.06E+07	4.34E-12	1.25	2.18E+08
Scan-0Ύ̇	Cpx	1.29E-10	0.30E-10	1.98E+07	9.62E-12	1.17	1.84E+08
Scan-HΎ̇	Fe-Spl	5.55E-11	0.40E-11	2.88E+07	1.29E-12	1.44	1.38E+08
Scan-LΎ̇	Fe-Spl	6.64E-11	0.51E-11	2.83E+07	1.14E-12	1.25	1.41E+08
Scan-0Ύ̇	Fe-Spl	5.14E-11	0.66E-11	2.85E+07	2.25E-12	1.17	1.26E+08

Table 2 – Average nucleation (J_M), maximum growth (G_{MAX}) rates and crystal number density (N_A) for all the mineral phases in the 3 scans, the Pl CPO strength is also reported together with the shear strain rate (Scan; HΎ̇, LΎ̇ and 0Ύ̇) domain. Standard error (SE) for G has been calculated from the ten largest crystals in each map, reflecting the precision of the mean estimate. J uncertainties (σJ_M) include propagated error from crystal size correction and crystal count.

Table 3 – Cluster chemical composition

Crystal	cluster	SiO_2	TiO_2	Al_2O_3	MnO	CaO	Na_2O	FeO	MgO	K_2O	Phase
Cpx	CLc1	49.34	1.17	4.68	0.14	20.69	0.33	7.13	16.06	0	Wo_{42}
	CLc2	44.99	2.21	7.58	0.12	21.44	0.46	9.15	13.1	0	Wo_{46}
	CLc3	47.89	1.54	5.86	0.14	21.42	0.44	7.71	14.57	0	Wo_{45}
Pl	CLp1	52.35	0	28.31	0	12.32	3.87	1.76	0	0.55	An_{62}
	CLp2	50.84	0	28.69	0	13.52	3.37	2.09	0	0.39	An_{67}
	CLp3	50.73	0	28.87	0	13.73	3.33	2.61	0	0.39	An_{68}
Fe-Spl	CLs1	0.13	4.2	7.9	0.53	0.17	0	69.56	11.9	0	Mfr_{53}
	CLs2	0.08	14.62	1.88	0.25	0.33	0	69.97	5.49	0	Mt_{60} (Ti-Rich)

Table 3 – Average chemical composition of each unique compositional cluster for each mineral phase.